DYNAMIC MODELS OF NON-FARADAIC ELECTROCHEMICAL SENSORS FOR POLYELECTROLYES

A Dissertation

Presented to the Faculty of the Graduate School

of Cornell University

In Partial Fulfillment of the Requirements for the Degree of

Doctor of Philosophy

by

Philip Hayes Gordon

January 2017

DYNAMIC MODELS OF NON-FARADAIC ELECTROCHEMICAL SENSORS FOR POLYELECTROLYES

Philip Hayes Gordon, Ph.D.

Cornell University 2017

BIOGRAPHICAL SKETCH

Philip Hayes Gordon was born in New Hartford, NY in 1988. The eldest of three children raised in that town by Dean and Mary Hayes Gordon, he worked in IT support for the school district before enrolling in Tufts School of Engineering. At Tufts he received a bachelor of science in electrical engineering with a minor in physics, while working for the Center for Engineering Educational Outreach, and interning at MIT Lincoln Laboratory. Graduating in 2010, he enrolled in the PhD electrical engineering program at Cornell University, which comes to fruition in the pages that follow. Aside from engineering he enjoys the study of sciences, history, and philosophy. For leisure he enjoys sports including (but not limited to) rugby, soccer, hockey, golf, weight-lifting, and running.

"Don't Panic"

- Douglas Adams, *The Hitchhiker's Guide to the Galaxy*

ACKNOWLEDGEMENTS

To my labmates, for their conversation, friendship, and advice.

To my friends and teammates for their support and making every day enjoyable.

To Edwin, for the help, encouragement, and wisdom.

To my siblings and grandparents for their great love and support.

To Mom and Dad, for their constant love and support.

TABLE OF CONTENTS

BIOGRAPHICAL SKETCH iii

ACKNOWLEDGEMENTS v

TABLE OF CONTENTS vi

LIST OF FIGURES ix

LIST OF TABLES xv

LIST OF ABBREVIATIONS xvi

LIST OF SYMBOLS xvii

CHAPTER 1 - CMOS BASED ELECTROCHEMICAL SENSORS 1

1.1 Introduction 1

1.2 The Ion Sensitive Field Effect Transistor (ISFET) 2

1.3 The Chemoreceptive Neuron MOSFET (CvMOS) 2

1.4 Interfacial Electrochemical Models 5

1.4.1 Introduction 5

1.4.2 Electrochemical potential 5

1.5 The Electrical Double Layer 7

1.5.1 Gouy and Chapman 7

1.5.2 Stern's Layer 8

1.5.3 Steric Modification 8

1.6 Contribution 9

CHAPTER 2 - NON-FARADAIC ELECTROCHEMICAL SENSING 11

2.1 Sensing Surface and Passivation 11

2.1.1 Surface Potential Response to pH 11

2.1.2 Ion Diffusion Concerns 12
2.2 Sensing Modalities 15
2.2.1 Transient Drain Current 15
2.2.2 Quasi-Static Gate Sweep 15
2.2.3 Impedance Spectroscopy 17
2.2.4 Capacitance vs. Voltage 19
2.3 A Hierarchical Extraction Method 21
2.3.1 The Circuit Model 21
2.3.2 Method of extraction 23
2.3.3 Results 24
CHAPTER 3 - THE IONIC DRIFT-DIFFUSION TRANSPORT CLOSE TO THE STERIC LIMIT 26
3.1 Abstract 26
3.2 Introduction 26
3.3 Mean Free Path from the Ideal Gas Theory 28
3.4 Implementation and Parameter Extraction 34
3.5 Conclusion 39
CHAPTER 4 - STERIC POLYELECTROLYTE EBBED DRIFT-DIFFUSION 40
4.1 Abstract 40
4.2 Introduction 40
4.3 Size Modified Poisson-Boltzmann Equations for Polyelectrolytes 41
4.4 Gridding and Stability 44
4.5 Parametric Variations 49
4.5.1 a_i - The effect of the Steric parameter 49

4.5.2 The Effect of Ebbed Diffusivity on Transient Ion Concentration 50
4.5.3 Approximations in a mono-electrolyte 51
4.5.4 Approximations for a Physiological Saline Solution 54
4.6 Experimental Observations 56
4.7 Conclusion 60
CHAPTER 5 - FABRIC BASED RFID ANTENNAE AND SYSTEMS 61
5.1 Introduction 61
5.2 Motivation 61
5.3 Fabrication 62
5.4 Testing 63
5.5 Conclusions 67
CHAPTER 6 - COMPARISONS AND ANALYSIS 68
6.1 Comparison to Other Models 68
6.2 SPEEDD Model Improvements and Additions 71
6.3 Conclusion 73
REFERENCES 74

LIST OF FIGURES

Figure 1.1 The ISFET structure compared to a standard MOSFET. The gate is exposed to solution allowing ions in the electrolyte to influence the channel formation [3]. 2

Figure 1.2 The CvMOS structure. The larger size of the Sensing Gate compared to the Control Gate indicates Csg > Ccg 4

Figure 1.3 The CvMOS diagram for circuit understanding. V_{cg} and V_{RE} provide voltage biases to the floating gate, which creates the channel through the oxide capacitance (C_{ox}). A parasitic capacitance from the bulk silicon of the chip, as well as line capacitances increases the overall capacitance, and must be taken into account in device sizing. 4

Figure 2.1 (Top) The CvMOS diagram for circuit understanding with a separate electrode chip wirebonded for an alternative sensing surface. The parasitic capacitance is significantly increased. The dotted line in the schematic represents the standard Ag/AgCl reference electrode setup, while the solid line represents the ability to use an on-chip pseudo-reference electrode. (Bottom) A plot of the capacitive path from V_{RE} to the floating gate and C_{para} versus the percentage of V_{RE} seen at the floating gate. 14

Figure 2.2 (Top) pH response of the extended Pt SG gate with (a) an Ag/AgCl reference electrode as the gate. Deviation from 59mv/pH indicates a capacitive ratio between the C_{sg} and C_T of 57%. (Bottom) IV data for polyelectrolyte mix, Ag/AgCl reference electrode to an Au sensing gate. Measurements are solid lines, and the model fit is the black circles. Negligible threshold shifts in different solutions indicate very little surface charge change, as shown in expanded inset. V_{ds} = 1V. 16

Figure 2.3 Bode response of CνMOS to different salinity NaCl. The time constant estimated for the 0.1mM solution by the dotted line. The green arrow shows the pole shifting to lower frequencies as solution concentration decreases, but R_{sol} and C_{DL} shifts cannot be decoupled by bode magnitude response alone. 18

Figure 2.4 CV of logarithmically varying $MgCl_2$ saline concentrations, measured on a 100µm x 100µm Au pad from an Ag/AgCl reference electrode. As the salinity increases, C_{DL} increases, and its intricacies become clearer. 20

Figure 2.5 CV of 50mM NaCl (30mV at 10kHz perturbation), compared to a PB and SMPB model. 21

Figure 2.6 Combined model for hierarchical extraction. The circuit model (on the left in red) represents the CνMOS governed by the equations described in chapter 1. In addition, there is a trace line resistance (R_{line}) and the parasitic capacitance (C_{para}) to be considered. The electrochemical model (on the right in blue) describes the circuit elements of the electrolyte and electrode systems. The reference electrode and non-Faradaic sensing electrode are governed by non-linear elements influenced by the composition of the electrode (*Mat*), the net molarity of the solution (M_{net}), the specific ionic species and their concentrations (c_i), and the voltage applied to the solution (V_{RE}). 22

Figure 2.7 CV experiments, measured from a on a 100µm x 100µm Au electrode to a reference Ag/AgCl electrode. Shown is 100mM $MgCl_2$. Swept 4 times both ascending and descending in bias voltage, the average capacitance of each sweep was taken and fitted to the f^{α} model for the impedance spectroscopy fit. Best fit for this experiment was α = -.51. 24

Figure 3.1 (Left) SMPB prediction of net charge profiles of ions extending from a charged non-faradaic electrode (x = 0nm) to a grounded bulk solution of 100mM NaCl with a_{Cl^-} = 7.8Å and a_{Na^+} = 7.0Å. The surface potentials vary from 500mV (lowest curves) to -500mV (highest curve) in 67mV steps. The slightly higher ionic size of a_{Cl^-} establishes a lower maximum interface concentration at positive surface potentials. (Right) Corresponding electrostatic potential profiles. 28

Figure 3.2 (a) Concentration profiles for two molarities of NaCl, showing a steric layer forming for the 100mM but not 1mM NaCl. Mobility and Diffusivity versus distance with surface potential at 300mV for: (b) 100mM NaCl and (c) 1mM NaCl. (d) Concentration of Na+ vs. distance for steady state solution after 300mV step for variation of ai in the SMPB and DD portions of the simulation. Lowering the DD ai in Eq. (3.17) will adjust the interface concentration, while lowering the SMPB ai in Eq. (3.16) does not, indicating that the Einstein relation in Eq. (3.13) is the critical modification to set the steric hindrance maximum. 35

Figure 3.3 (a) Staircase bias experiments of 100mM NaCl with pulses in 50mV increments from 50mV to 300mV. (b) Filtered transient current of each pulse overlaid, with single time constant fitting. Significant deviation from exponential occurs between 100 and 150mV. (c) COMSOL staircase bias simulation from 70-130mV with normalized root-mean-square error (RMSE) of exponential fitting versus pulse height. As the pulse height increases, the steric effects begin to cause the current response to deviate from a single-time-constant response. Experimental data of 100mM NaCl indicate Na^+ effective ionic size can be best fit by a_i = 0.70nm. (d) Current density vs. distance for the drift and diffusive fluxes of the Na^+ ion transport during the bias step from 300mV to -300mV. The curved arrows indicate the progression of the current density for time steps 2-7 in the inset. (e) Transient concentration profiles and (f) Transient potential profiles for time steps 1-7. 38

Figure 4.1 Simulation results for polarizable and non-polarizable electrode boundary conditions, stimulated by a -300mV pulse for a 100mM NaCl and 50mM $MgCl_2$ mixture. (Top) Interface concentrations at the grounded, polarizable electrode, showing Cl^- ions piling up at the surface. (Bottom Left) Concentration at the driving electrode. The polarizable electrode shows decrease in concentration, while the non-polarizable electrode shows a slight increase in concentration indicating a flux of Cl^- ions into the solution. (Bottom Right) Time derivative of concentration near the driving electrode. 46

Figure 4.2 Convergence properties of modified (M) and constant or uncorrected (U) Einstein relations for a 300mV step for 2nm and .2nm discretization near the interface. For 2nm discretization with $a_i \sim .7$nm, both the corrected and constant Einstein relation simulations converge to similar solutions, however for the .2nm discretization, the constant Einstein relation fails to converge (oscillating solid red curve continues to oscillate until an exception is thrown), while the corrected system yields the same solution but with a finer mesh. The time step change number indicates each time during the course of the solution that the time step had to be adapted. 48

Figure 4.3 Effect of varying a_{Mg} 3Å to 12Å, from COMSOL simulation. As a_{Mg} increases, the maximum concentration possible at the interface decreases, and the Steric layer extends further into solution. Bulk concentration is 100mM = 100 mol/m^3, and φ=300mV at the interface x = 0m. 49

Figure 4.4 Effect of varying a_{Mg} between 7.8Å, 9.8Å, and 11.8Å. As a_{Mg} increases, the net current seen through the solution decreases. 50

Figure 4.5 Interface concentrations (at the first grid-point 2nm from the interface) of the modified Einstein relation (left) and the constant or uncorrected Einstein relation (right) solutions to bipolar 400µs, 300mV bipolar pulses applied to 100 mol/m^3 NaCl. The mobility corrected solution reaches a steady state on the order of microseconds, while the uncorrected concentration continues to rise to unphysical concentration levels on a too long a time scale. 51

Figure 4.6 (Top) Full view of the 300mV bipolar pulsed experiment (RE and Au represent measurements from the reference electrode and gold electrode respectively, and are inverses of each-other minus an offset from the Keithley 4200 measuring unit. Only one is shown in future graphs). (Bottom Left) Zoomed view of the transition between neutral (excepting the built in potential difference) and negative surface potential. (Bottom Right) Zoomed view of transient currents and simulation resulting from a 70mV applied potential. 57

Figure 4.7 Experimental data for NaCl and $MgCl_2$ saline solutions of various molarities, combinations and ramp rates. (Top) Experimental data for a 300mV 10ms bipolar pulse, with initial ramp rates of 10μs and 100μs (yellow dotted lines). The different initial ramp rates may alter the composition of the double layer based on the relative mobilities and energetic favorability. (Middle): zoomed view of currents as the cation steric layer dissipates from the surface as the electrode potential difference returns to zero. The saline solution with 1mM $MgCl_2$ mixed with 100mM NaCl shows a longer decay current than the solution with only 100mM NaCl, as the less concentrated, lower mobility, but more energetically favorable Mg^{+2} moves away from the surface. (Bottom) zoomed view of currents as the anion steric layer dissipates from the surface. As this is composed of Cl^- for all solutions, no change is seen in the transient current profile, but the same increase in current for higher salinity is clear. 58

Figure 4.8 Interface Concentration profiles for 100mM NaCl (left) and 100mM NaCl + 10mM $MgCl_2$ subject to a 300mV anodic pulse followed by a 300mV cathodic pulse. For the mono-cation electrolyte, the concentrations rapidly approach steady state values, while the poly-cation electrolyte requires a long equilibration time as the higher mobility Na^+ initially forms the steric layer, and is then replaced by the more energetically favorable Mg^{+2}. 60

Figure 5.1 Photograph of commercial Smartrac® ShortDipole UHF RFID tag (top) next to the fabric based antenna with an IC chip connected in the center (bottom). The fabric antenna, while 15% larger and 300x higher resistance, still functioned similarly out to 2.5m. 63

Figure 5.2 Left) Received signal strength indicator (RSSI) vs. reading distance for both the embroidered fabric tag (red) and the commercial control tag (blue). Comparable performance was achieved out to 2.5m, before signal was lost for the embroidered antenna. Right) Embroidered antenna RSSI response to 100mM NaCl saline solution. Droplets were added until full saturation at droplet 7, after which recordings were taken until fully dry at marker 10. Partial wetness

decreased signal strength, which had worse performance than full saline saturation probably due to impedance mismatch. Returning to a dry state showed no lasting effects..... 64

Figure 5.3 Left) Received signal strength indicator (RSSI) vs. reading distance for both the embroidered fabric tag (red) and the commercial control tag (blue). Comparable performance was achieved out to 2.5m, before signal was lost for the embroidered antenna. Right) Embroidered antenna RSSI response to 100mM NaCl saline solution. Droplets were added until full saturation at droplet 7, after which recordings were taken until fully dry at marker 10. Partial wetness decreased signal strength, which had worse performance than full saline saturation probably due to impedance mismatch. Returning to a dry state showed no lasting effects..... 67

LIST OF TABLES

Table 2-1 Circuit parameters extracted for 20μL of 1mM NaCl added to 20μL of the solution in column 1. 25

Table 4-1 Decreasing rate of diffusivity by different terms in Eq. 4.8 with $A = l \cdot a = 50a^2$ 52

Table 4-2 Composition in typical biological buffers such as PBS 55

Table 5-1 Received Signal Strength Intensity during wear 65

Table 6-1 Model Comparisons 68

LIST OF ABBREVIATIONS

AC	Alternating Current
CG	Control Gate
CvMOS	Chemoreceptive Neuron MOSFET
CMOS	Complementary Metal-Oxide-Semiconductor
CV	Capacitance vs. Voltage
DC	Direct Current
EDL	Electrical Double Layer
ESG	Extended Sensing Gate
GCS	Gouy-Chapman-Stern
ISFET	Ion Sensitive Field Effect Transistor
IV	Drain Current vs. Gate Voltage
LIA	Lock-In Amplifier
MD	Molecular Dynamics
MOSCAP	Metal-Oxide-Semiconductor Capacitor
MOSFET	Metal-Oxide-Semiconductor Field Effect Transistor
PB	Poisson-Boltzmann
PBS	Phosphate-Buffered-Saline
QRE	Quasi Reference Electrode
RE	Reference Electrode
RFID	Radio Frequency Identification
SG	Sensing Gate
SMPB	Size Modified Poisson-Boltzmann
SNR	Signal to Noise Ratio
SPEEDD	Steric Polyelectrolyte Ebbed Drift-Diffusion
TIA	Trans-Impedance Amplifier

LIST OF SYMBOLS

Parameters

a_i	Ionic radius
C_{DL}	Double Layer Capacitance
C_t	Total Capacitance
D_i	Diffusivity
f	Frequency
F	Faraday's Constant = 96,487 C/mol
I_{ds}	Drain to Source current
k	Boltzmann Constant = $1.38064852 \cdot 10^{-23}$ J/K
N_A	Avogadro's Number = $6.0221409 \cdot 10^{23}$ mol^{-1}
q	Elementary Charge = $1.6021766208(98) \cdot 10^{-19}$ C
Q_i	Total charge on surface 'i'
R_{sol}	Solution Resistance
T	Temperature
V_{fg}	Floating Gate Voltage
V_T	Thermal Voltage
φ	Electric Potential - Voltage

CHAPTER 1

CMOS BASED ELECTROCHEMICAL SENSORS

1.1 Introduction

The explosion of the semiconductor industry over the past 70 years has ushered in revolutions in many fields of human endeavor. From communication to business, entertainment to education, it is a shorter list of fields that haven't changed than have.

With an estimated size of over $350 billion dollars [1] with decades of optimization and technological advancement invested in Complementary Metal-Oxide Semiconductor (CMOS), it is pragmatic to look for areas other than computation to apply the advances. Electrochemical sensing seems a field ripe for this transition. With the nano-resolution methods available to create devices, sensing on the scales of cells, organelles, proteins, DNA, or single molecules becomes viable.

Sensing electrochemical species relevant to biology, however, requires interfacing CMOS components with ions in water, which is traditionally a death sentence for integrated electronics. Furthermore, the electrochemistry involved in the solid-liquid interface must be well understood to separate signal from noise.

1.2 The Ion Sensitive Field Effect Transistor (ISFET)

The ISFET, introduced in 1970 by Piet Bergveld is the most general CMOS based interfacial sensor [2]. A field effect transistor with a gate open to solution, and current through the device controlled by the electric field at the interface (Figure 1.1).

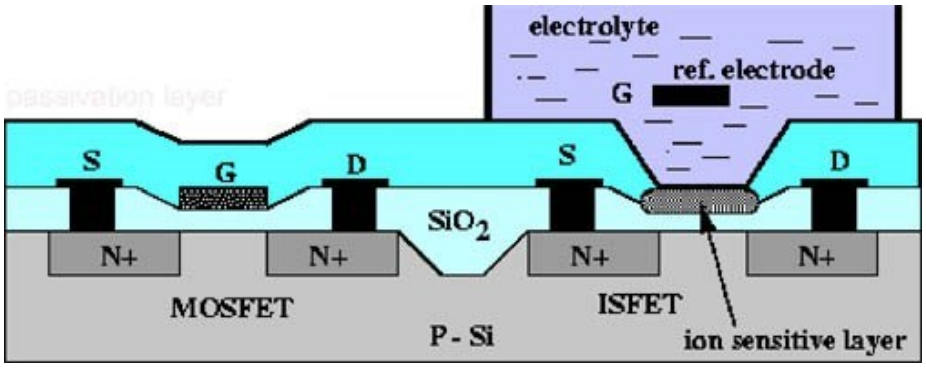

Figure 1.1 The ISFET structure compared to a standard MOSFET. The gate is exposed to solution allowing ions in the electrolyte to influence the channel formation [3].

'Ion Sensitive' indicates that charged species in solution contribute to the operation of the device.

1.3 The Chemoreceptive Neuron MOSFET (CvMOS)

A new flavor on the ISFET was the CvMOS, introduced by Shibata and Ohmi in 1992 [4]. A flash memory transistor consisting of multiple gates capacitively coupled to an extended floating gate, which controls the charge creating the channel. The floating gate is a conductive area (polysilicon generally), above the channel, which is

electrically isolated, but close enough to a controlled electrical region to enable charge tunneling.

By selecting different coverage areas (or dielectrics or dielectric thicknesses) for different gates, the strength of the capacitive coupling of each gate relative to the others can be modulated (this operation inspired the 'neuron' in the naming, as multiple weighted electrochemical input signals control a single output). Particularly, for electrochemical sensing a dual-gate CvMOS is utilized, with one gate open to solution for sensing, and the other with an electrical contact available to bias the floating gate to the most appropriate operating region.

Governed by Eqs. 1.1-1.4, The structure of the CvMOS is shown in Figure 1.2, and the circuit layout for general experiments in Figure 1.3.

$$V_{fg} = \frac{Q_{fg}}{C_t} + \frac{Q_{surf}}{C_t} + \frac{C_{gd}V_{ds}}{C_t} + \frac{C_{sg}V_{sg}}{C_t} \quad (1.1)$$

$$C_t = C_{ox}||C_{dep} + C_{bulk} + C_{gs} + C_{gd} + C_{sg} + C_{para} \quad (1.2)$$

$$I_d = k\frac{W}{L}e^{\frac{\frac{C_{ox}}{C_t}(V_{fg}-V_{th})}{V_T}} \quad (1.3)$$

$$I_d = k\frac{W}{L}[(V_{fg} - V_{th})V_{ds} - .5V_{ds}^2] \quad (1.4)$$

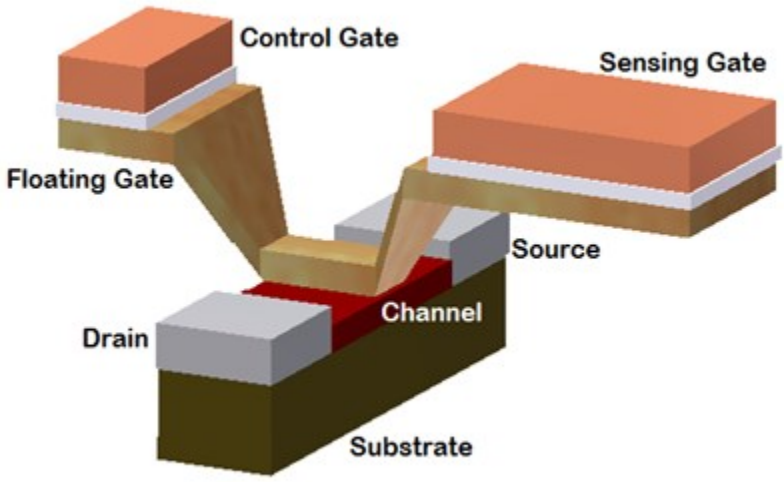

Figure 1.2 The CvMOS structure. The larger size of the Sensing Gate compared to the Control Gate indicates Csg > Ccg

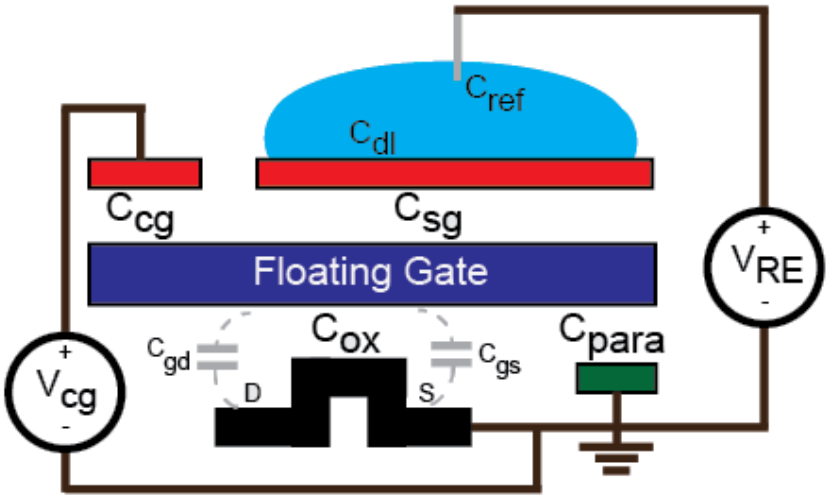

Figure 1.3 The CvMOS diagram for circuit understanding. V_{cg} and V_{RE} provide voltage biases to the floating gate, which creates the channel through the oxide capacitance (C_{ox}). A parasitic capacitance from the bulk silicon of the chip, as well as line capacitances increases the overall capacitance, and must be taken into account in device sizing.

1.4 Interfacial Electrochemical Models

1.4.1 Introduction

The equilibration of boundary conditions between materials must be understood for efficiency in any sensor system. The electrical and chemical interactions between a solid boundary and an aqueous solution contain many charge varieties which combine to satisfy the coupled mechanical, electrical, and chemical equilibrations.

Dissociated salts in water create a saline solution, with the individual ions as well as dissociated hydrogen ions allow for charge transfer through an aqueous solution, as electrons allow for current in a conductor.

Interfaces can be divided into two types: Faradaic, which has a charge transfer mechanism at the interface allowing for a DC current to flow, and Non-Faradaic, which has no charge transfer species, and thus forms a capacitive coupling at the interface with built up charge on either side creating a potential difference.

The distribution of electrical charge in a potential profile is the governing force involved in the system, and is described by Poisson's Eq. 1.5.

$$\nabla^2 \varphi = \frac{\rho}{\epsilon} \qquad (1.5)$$

1.4.2 Electrochemical potential

When dealing with ionic species in water under electrical stimulus, the concept of the potential driving the species must be scrutinized in detail. The driving forces of a charged species are the electric potential at its point in space (φ), as well as the

chemical potential (μ_{chem}) relating to the concentration of the species in solution (n_i, the concentration of particles in m^{-3}), as shown in Eqs. 1.6 and 1.7.

$$\bar{\mu_i} = z_i F\varphi + \mu_{chem_i} \quad (1.6)$$

$$\mu_{chem_i} = \mu^0_{chem_i} + \frac{kT}{q} ln\left(\frac{n_i}{n_{tot}}\right) \quad (1.7)$$

The charge of each species is encountered is z_i, and Faraday's constant (F) is the net charge of one mole of an elementary charge.

In typical electronic systems, electrons are the charge carriers which deliver current through the entire system, with a conductive solid such as copper providing a path between components. In an electrolyte, however, electrons are not the charge carrier, as electron transfer with water must result in a reduction or oxidation reaction, with either the water or species in solution (this charge transfer defines a Faradaic electrode) [5].

As the charge carrying species will shift from electron, to ions, and back through an electrode-electrolyte system, the establishment of a steady state electrochemical equilibrium is no longer assured. If a charge transfer mechanism is unavailable between the solid and liquid phases, the system will reach an electrochemical equilibrium, but the individual contributions of the chemical potential and electric potential cannot be separated, making the solution electric potential ill-defined. Concerning circuit modeling and electrical experimentation, this is an unwelcome situation, and thus a reference electrode, or electrode with a charge transfer

mechanism to the solution is employed to establish a chemical potential equilibrium and give the bulk solution a well-defined electric potential.

1.5 The Electrical Double Layer

Unlike a traditional parallel-plate capacitor, with a dielectric between two conductors, the ions in solution approach the interface as closely as possible. Described by Hermann von Helmholtz [6], charged solids in an electrolyte environment will attract ions of the opposite charge (counter-ions) and repel similarly charged ions (co-ions) in an area near their surface [7]. The combination of an electric field driving ions to the interface, and like-ion repulsion leads to a large buildup of charge on the surface, with the charge density tapering off into solution in a more diffuse layer extending into the solution.

This formation is called the electrical double layer (EDL), and the more precise the description available, the more clearly sensor readings can be understood.

1.5.1 Gouy and Chapman

The next significant progress made in the description of the EDL was presented just over a century ago as Louis Georges Gouy, and David Leonard Chapman both examined further the capacitive properties of solid-electrolyte systems [8, 9].

Observing that the capacitance was not independent of the voltage on the solid, both postulated a diffuse layer of co-ions extending into the solution. This layer was

described by Maxwell-Boltzmann statistics, giving a Poisson-Boltzmann (PB) description of the EDL, governed by Eqs. 1.8 and 1.9.

$$\nabla^2\varphi = \frac{-q}{\varepsilon}\sum_i z_i N_A c_i \qquad (1.8)$$

$$c_i = c_i^b e^{-z_i\varphi/V_T} \qquad (1.9)$$

1.5.2 Stern's Layer

In an effort to remedy the unphysical predictions of the Gouy-Chapman model near the interface, Stern proposed two explicitly different regions the EDL, with the area immediately adjacent to the surface (like the capacitance described by Helmholtz) being a constant capacitance, and the diffuse layer beyond obeying the Gouy-Chapman model [10]. The composite of these models is referred to as the Gouy-Chapman-Stern (GCS) model.

1.5.3 Steric Modification

The addition of the Stern layer describes a densely packed layer of ions close to the surface of the solid. To incorporate the immobile layer into a PB description, a steric modification is added to the concentration term. Invoking an effective ionic cross-section (a_i), a maximum concentration determined by packing density is described by Eq. 1.10.

$$c_i = \frac{c_i^b e^{-z_i\varphi/V_T}}{1 + \sum_i a_j c_{j_0} e^{-z_i\varphi/V_T}} \qquad (1.10)$$

$$c_i = \frac{n_i}{N_A} \qquad (1.11)$$

The relationship between concentrations is added in Eq. 1.11 for clarification, as sometimes it is simpler to speak of molar concentration (c_i in mol/m^3) and other times in net concentration of particles (n_i in m^{-3}).

Eqs. 1.8 and 1.10 form the basis for the Size Modified Poisson Boltzmann (SMPB) model, which provides an equilibrium solution for an EDL concentration profile, and electrochemical potential [11, 12].

1.6 Contribution

First, to assist the design process of non-Faradic electrochemical sensors in realistic biological media, we examine multiple types of sensing operations in polyelectrolytes. By comparing the quasi-static transconductance, impedance spectroscopy, and capacitance-voltage (CV) measurements, we assess the physical contributions from the double layer composition, overall solution resistance, and sensing surface potential under various poly-electrolytic molarities. The mixture of NaCl and $MgCl_2$ is chosen for illustration to provide insight into circuit model parameters for non-Faradaic sensing. Our finding also sheds light on the dynamics of double-layer competition and correlation, which is critical for understanding the physical phenomena occurring at the sensing interface, and accurately interpreting sensor data.

Secondly, a new mean field model is implemented for the purpose of accurately predicting the behavior of non-Faradaic electrochemical sensors. The goal of this

model is to accurately predict the behavior of non-Faradaic electrochemical sensors beyond the state of the art [13-15].

CHAPTER 2

NON-FARADAIC ELECTROCHEMICAL SENSING

2.1 Sensing Surface and Passivation

2.1.1 Surface Potential Response to pH

The choice of sensing interface for a CMOS based electrochemical sensor must be based on the type or types of measurements intended. The most basic choice is whether to use an insulator or a conductive metal as the sensing surface.

Insulators such as oxides and nitrides provide the best pH response, and are the interface of choice for ISFET based pH sensors. The amphoteric nature of the interface bonds allow for covalent bonding of both H^+ and OH^- to the material making up the insulator*. All other things equal, the pH, or concentration of the H^+ ions in solution determine the potential at the amphoteric interface by the Nernst equation, Eq. 2.1.

$$\varphi_{sg} = \varphi_0 + \alpha \frac{kT}{q} \ln(a_{H^+}) = \varphi_0 + \alpha * (59mV) * \log(a_{H^+}) \qquad (2.1)$$

As the exact initial potential offset due to initial conditions for a given system (φ_0) is generally not known, and calibration is generally required for pH sensing. However, the response of the surface to a given change in pH is described in Eq. 2.2.

* In this work, the insulators considered are silicon dioxide (SiO_2) and silicon nitride (Si_3N_4), however many other materials are currently in use for ISFET based pH sensing such as TaO_5, GaN and AlN.

$$\frac{\partial \varphi_{sg}}{\partial pH} = \varphi_0 + \alpha \frac{kT}{q} \ln(a_{H^+}) = \alpha * (59mV) \qquad (2.2)$$

This 59mV per change in pH level (or decade change in H^+ concentration) is known as a Nernstian response. The parameter α indicates how far a material deviates from this general response, generally varying between 0 and 1[†]. For pH sensing, a high α is desirable, but for other sensing modalities, changes in pH may reduce the signal to noise ratio (SNR).

The CvMOS offers unique benefits in terms of surface conditioning. By biasing adjusting the charge on the floating gate, the interface potential can be shifted around the point-of-zero-charge of the surface, increasing or decreasing sensitivity to pH changes. This and many other surface sensing intricacies are probed in depth in Jayant et. al. [16-18].

2.1.2 Ion Diffusion Concerns

In addition to pH sensitivity, the ability of ions from salts to diffuse into an insulator or silicon presents a major design consideration for ISFETs. Anything but the most pristine oxides and nitrides will provide defects for ionic species to penetrate into the device [19, 20]. This causes not only noise in the current measurement, but a source of noise in all future measurements on a diffusive time scale significantly

[†] Many claims have been made about Super-Nernstian ($\alpha > 1$) surfaces and devices, though most seem to rely on simple amplification. For instance, the CvMOS device can exhibit apparent changes in surface potential well in excess of 59mV/pH, but is simply the capacitive amplification from the relative sizing of the sensing and control gates.

different than the solution. In addition, being in the insulator itself, each charge has an unknown capacitive effect on the channel, as the distance to the channel is unknown.

With these challenges in mind, for non-pH sensing systems, an external electrode chip can be utilized, creating an extended sensing gate (ESG) setup. Only feasible with a metal SG, a wirebonded connection can be made to an electrode of a second chip, ensuring that any ion diffusion will not compromise the semiconductor device chip.

Such an ESG setup must naturally contribute additional parasitic circuit elements, and it must be the design engineer's task to assess if the additional capacitive load will compromise the sensing fidelity. The parasitic capacitance's effect on the overall signal from the reference electrode, as well as a schematic setup for an ESG device is shown in Figure 2.1.

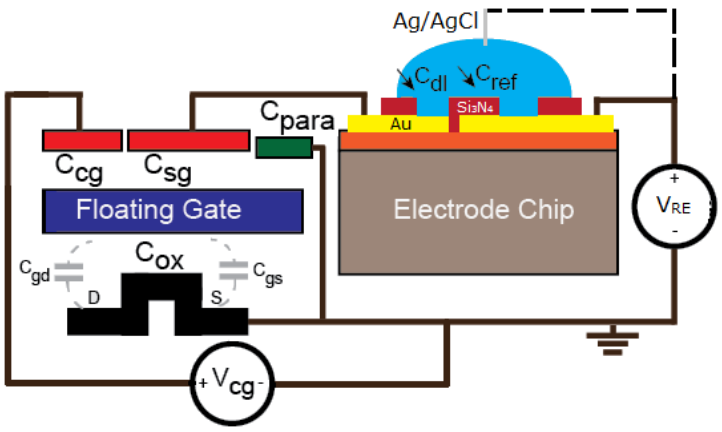

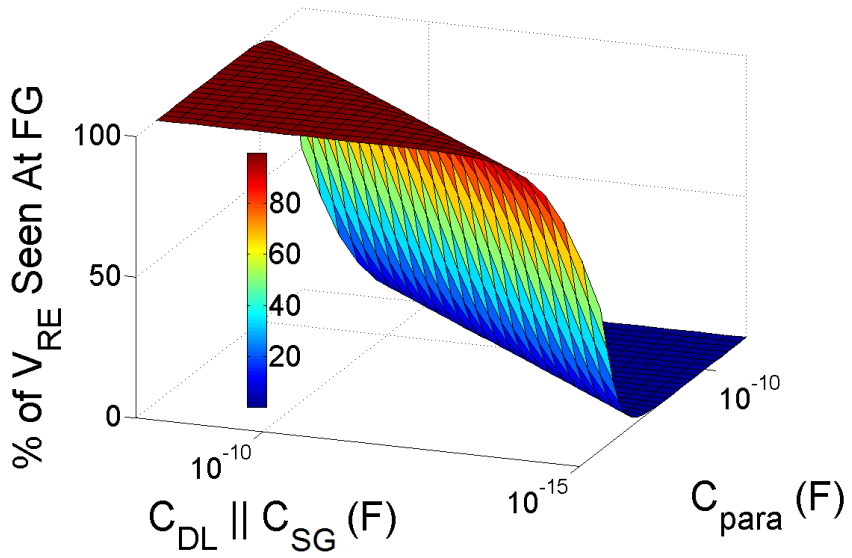

Figure 2.1 (Top) The CνMOS diagram for circuit understanding with a separate electrode chip wirebonded for an alternative sensing surface. The parasitic capacitance is significantly increased. The dotted line in the schematic represents the standard Ag/AgCl reference electrode setup, while the solid line represents the ability to use an on-chip pseudo-reference electrode. (Bottom) A plot of the capacitive path from V_{RE} to the floating gate and C_{para} versus the percentage of V_{RE} seen at the floating gate.

It is clear from Figure 2.1 that a large parasitic capacitance can completely obfuscate any signal from a reference electrode, if the series capacitance of the double layer and sensing gate is not sufficiently high. However, there is a design space where practically all of V_{RE} is seen at the floating gate, and for almost all saline conditions (C_{DL} sufficiently high), and a wirebonding length < 5cm and this can be achieved by sizing the sensing gate appropriately [21].

2.2 Sensing Modalities

2.2.1 Transient Drain Current

Many modalities of sensing are available in ISFET style devices. The most intuitive a transient current measurement, which is to say to bias the device, and measure the drain current (I_d), as it changes over time. This is the current from drain to source (I_{ds}) if the device is operating properly. This gives a measure of voltage at the sensor interface by the current/voltage relationship of the transistor in a given operating regime. Proper biasing is thus paramount for the interpretation of experimental results.

2.2.2 Quasi-Static Gate Sweep

The biasing conditions of the transistor lead to another sensing option, of sweeping a gate voltage and measuring the current (Vgs vs. I_d or simply IV). A quasi-static method in nature, the IV measurement will yield a subthreshold slope, and a threshold voltage for the transistor. The subthreshold slope indicates the change in voltage required for a tenfold increase in current, and remains constant in the subthreshold regime due to the exponential relationship between current and voltage [22]. This gives a measure of the relative capacitance values between the gate being swept, and all other capacitances affecting the channel, and helps determine the maximum sensitivity of the device.

The threshold voltage can be defined a number of ways, but is at heart a measure of essentially when the device ‘turns on’. In this work, it will be taken as the bias voltage at which the transistor delivers 1μA, for a given drain to source bias. Charge at the

interface of the sensing gate, and also on the floating gate of the CvMOS, will shift the threshold voltage, and a measurement of that charge can be determined from a known capacitance measurement as shown in Eq. 1.1. Using the IV measurement, solution parameters such as pH can be determined by threshold shift, while other parameters (such as salinity) will show negligible effect, as shown in Figure 2.2

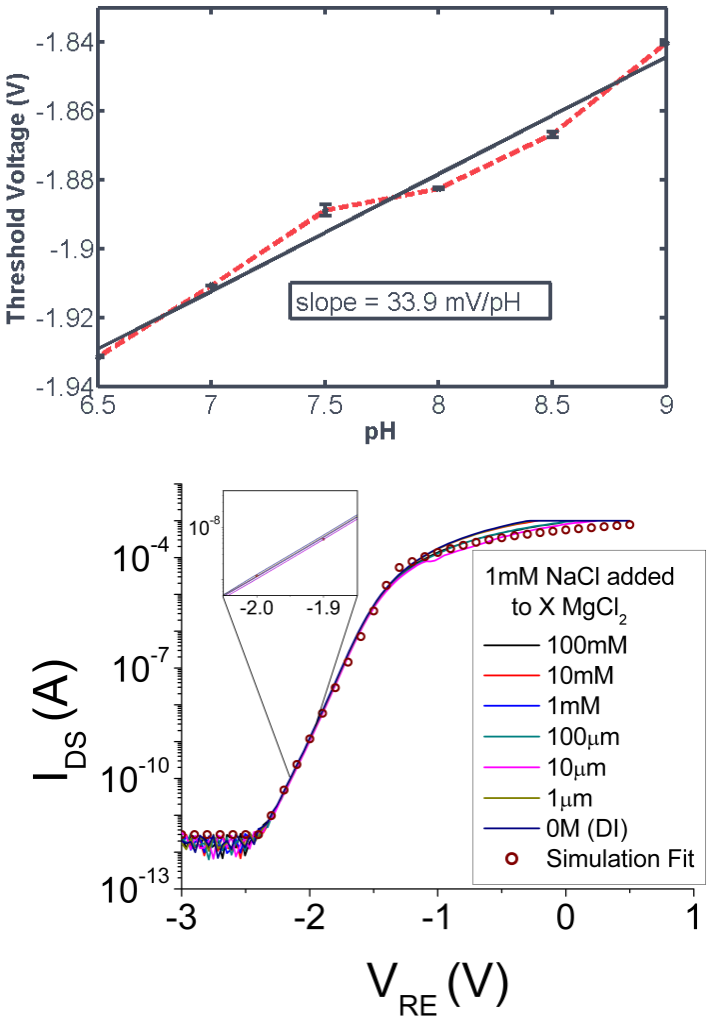

Figure 2.2 (Top) pH response of the extended Pt SG gate with (a) an Ag/AgCl reference electrode as the gate. Deviation from 59mv/pH indicates a capacitive ratio between the C_{sg} and C_T of 57%. (Bottom) IV data for polyelectrolyte mix,

Ag/AgCl reference electrode to an Au sensing gate. Measurements are solid lines, and the model fit is the black circles. Negligible threshold shifts in different solutions indicate very little surface charge change, as shown in expanded inset. V_{ds} = 1V.

2.2.3 Impedance Spectroscopy

While DC measurements yield mainly surface information, higher frequency measurements can sense further into a solution. Impedance spectroscopy consists of applying a small signal (V_{AC} < 100mV) AC perturbation to the solution and measuring the response received either in the form of voltage from another electrode, or current through an ISFET. For the electrode-to-electrode setup, a lock-in amplifier (LIA) is used to measure the signal received through solution, allowing for vastly improved SNR compared to a traditional voltage measurement. For an ISFET setup, the current is passed through a trans-impedance amplifier (TIA), and then to the lock-in for high fidelity sensing.

By sweeping through a logarithmically distributed number of voltages a bode plot, such as that shown in Figure 2.3, can be created, showing how the magnitude and phase of the signal transduction changes with respect to frequency. This gives information concerning the resistivity of the solution (R_{sol}), the double layer capacitance (C_{DL}) from the dominant time constant ($\tau = RC$), and various relaxations of molecules in the solution [23]. In conjunction with a capacitance vs. voltage measurements, values for R_{sol} and C_{DL} can be extracted.

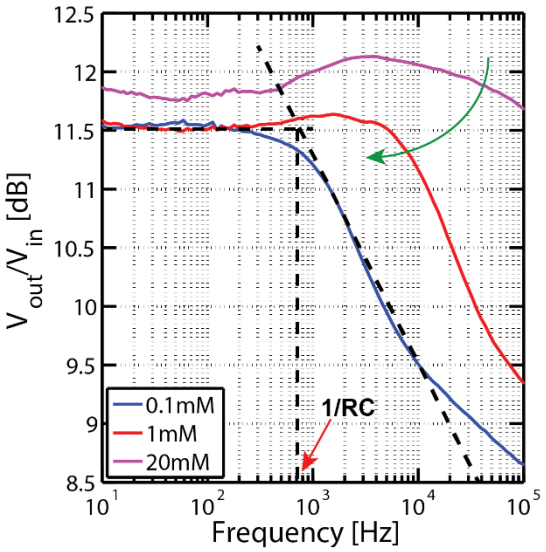

Figure 2.3 Bode response of CvMOS to different salinity NaCl. The time constant estimated for the 0.1mM solution by the dotted line. The green arrow shows the pole shifting to lower frequencies as solution concentration decreases, but R_{sol} and C_{DL} shifts cannot be decoupled by bode magnitude response alone.

The model used to analyze this non-Faradaic impedance spectroscopy setup is described in Eqs. 2.3 and 2.4.

$$H(s) = M_0 / \left[\frac{1}{1 + sR_{sol}C(c_i, f)} \mathrm{x} \frac{1}{1 + sR_{sol}C_0}\right] \qquad (2.3)$$

$$C(c_i, f) = C(c_i) f^{\alpha} \qquad (2.4)$$

The loss due to resistive division is M_0, and the solution resistance is R_{sol}. $C(c_i, f)$ depends on frequency and ion concentrations, α is a fitting parameter for the frequency dependence of the double layer capacitance, and C_0 is a non-frequency dependent capacitance. This differs from a traditional Warburg impedance model (or constant-phase-element) by explicitly differentiating a non-frequency dependent capacitance,

and a non-linear capacitance [24]. This is in keeping with a Gouy-Chapman-Stern view of the EDL, with a constant capacitive layer at the interface, and a diffuse capacitance extending into solution.

2.2.4 Capacitance vs. Voltage

Almost a hybrid of the gate sweep and impedance spectroscopy is the Capacitance vs. Voltage measurement (CV). An important measurement for metal-oxide-semiconductor capacitors (MOSCAPs), a small AC perturbation is applied as the DC voltage is swept. The change in charge is measured, and the differential capacitance is calculated[‡], as per Eq. 2.5.

$$C_{diff} = \frac{dq}{dV} \qquad (2.5)$$

The CV is electrode based measurement, and while it can be run from an ISFET to sense a solution, it requires decoupling additional system capacitors which degrade the measurement. It is, however, useful for analysis of individual components of the system, such as the semiconductor alone, the properties of an oxide based electrode, or solution info in an electrode based system. Information available from a CV includes the overall differential capacitance (which can be C_{DL} depending on system setup), as well as information about the double layer composition.

[‡] There can be some confusion on the capacitance being measured, so it is important to note that the differential capacitance represents, a given bias voltage, the change in charge that will be observed for a given change in voltage. This is in contrast to an integral capacitance, which, at a given voltage, is a measure of the total charge that has accumulated at that voltage.

Peaks and troughs in the CV indicate more or less charge responding. As the DC bias is swept, the composition of the double layer changes, particularly if the sweep passes the PZC, and the majority ion switches from cation to anion (or vice-versa). The complexity of the CV measurement in electrolyte systems can be seen from Figure 2.4.

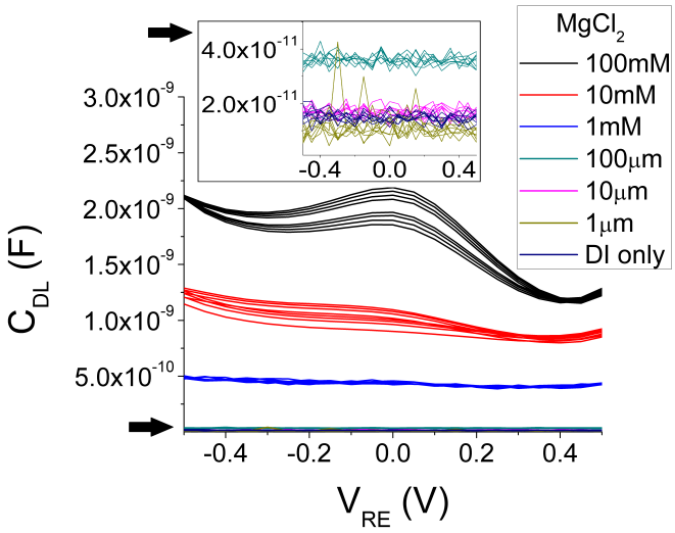

Figure 2.4 CV of logarithmically varying $MgCl_2$ saline concentrations, measured on a 100µm x 100µm Au pad from an Ag/AgCl reference electrode. As the salinity increases, C_{DL} increases, and its intricacies become clearer.

While the complex shape of these CV's have been understood [25, 26], a capacitance with both non-linear frequency and voltage elements, that varies significantly with the ions of its construction, is a difficult lumped circuit element to model simply. A simple implementation of the SMPB model described in section 1.5.3 can be implemented to approximate the capacitance expected based on the concentrations of the ions of the electrolyte, as shown in Figure 2.5.

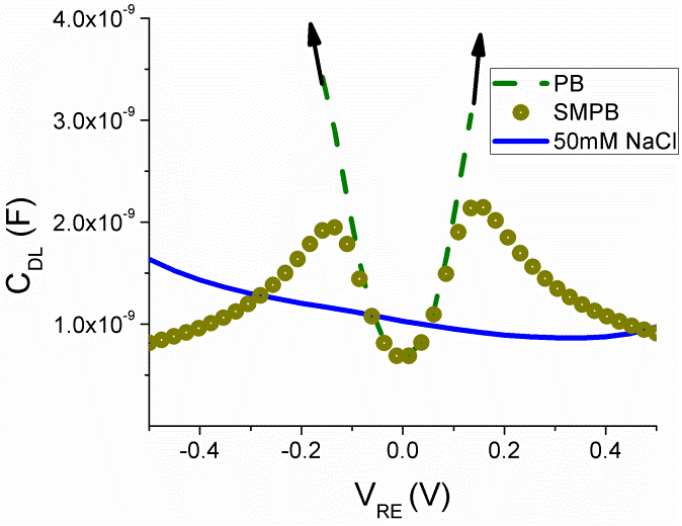

Figure 2.5 CV of 50mM NaCl (30mV at 10kHz perturbation), compared to a PB and SMPB model.

The PB model quickly estimates unrealistically high capacitance values, while the SMPB model gives an accurate order of magnitude, but incorrect qualitative fitting for ionic sizes (a_i) taken from tabulated sources addressing bulk conditions [27]. This qualitative inaccuracy is the first sign that a more in depth understanding of the interface electrochemistry is required for accurate experimental prediction, and will be addressed in detail in chapters 3 and 4.

2.3 A Hierarchical Extraction Method

2.3.1 The Circuit Model

While a very significant body of work has been done on models for ISFET measurements for measurement accuracy, very few attempt a model which takes multiple sensing modalities and integrates their extracted measurements [28-33]. For

any given sensing modality, the models of section 2.2, and others as well, can give accuracy (to varying degrees, but each useable for some sensing situation), but the difficulties and discrepancies can come from integrating models. Clearly, however, an experimental setup with multiple sensing modalities delivering information with some redundancy would be more reliable than a single result from a non-standard system. To this end a hierarchical experimental parameter extraction model is adopted for the sensing modalities. The combined circuit and electrochemical model is shown in Figure 2.6.

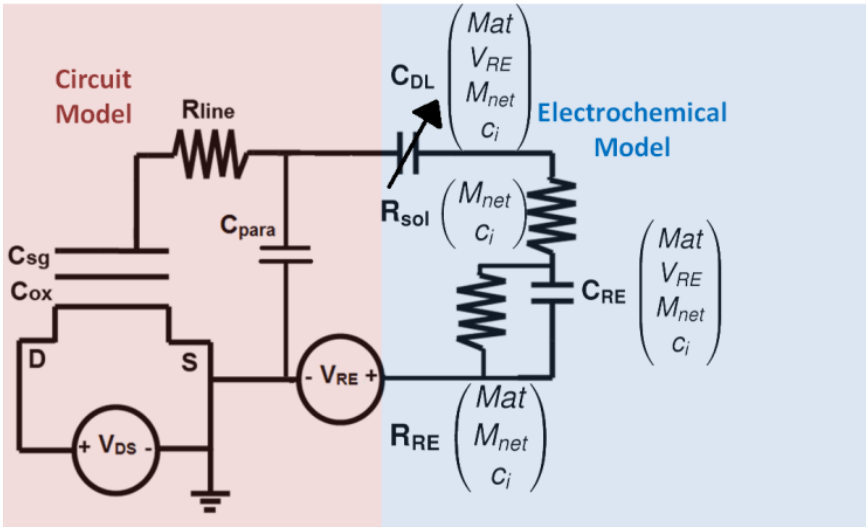

Figure 2.6 Combined model for hierarchical extraction. The circuit model (on the left in red) represents the CvMOS governed by the equations described in chapter 1. In addition, there is a trace line resistance (R_{line}) and the parasitic capacitance (C_{para}) to be considered. The electrochemical model (on the right in blue) describes the circuit elements of the electrolyte and electrode systems. The reference electrode and non-Faradaic sensing electrode are governed by non-linear elements influenced by the composition of the electrode (*Mat*), the net

molarity of the solution (M_{net}), the specific ionic species and their concentrations (c_i), and the voltage applied to the solution (V_{RE}).

2.3.2 Method of extraction

Given data from each of the sensing methods described in section 2.2, a parameter extraction algorithm was developed as follows:

- From a CV run at multiple frequencies (as shown in Figure 2.7), extract the non-frequency dependent double layer capacitance (C_0 from equation 2.3) from the highest frequency measurement, and the α (from Eq. 2.4), by the change of capacitance with respect to frequency.
- Using the capacitance parameters from the CV, fit the impedance spectroscopy data's dominant pole with the resistance involved being the net resistive path seen from the interface. The solution resistance (R_{sol}) is then that resistance minus any the line and reference electrode resistances.
- From an IV sweep and device design characteristics (particularly gate sizes and oxide thicknesses) The potential of the floating gate can be determined, and by the capacitive coupling described in Eqs. 1.1 and 1.2, the potential at the sensing gate surface (V_{sg}) can be determined.
- With these parameters in hand, a transient current measurement can be understood deeper in terms of surface potential shifts causing drift, or perturbation based measurements (i.e. adding or changing the state of the

solution as current is being measured), as basic time constants, resistances, and capacitances of the system have an established baseline.

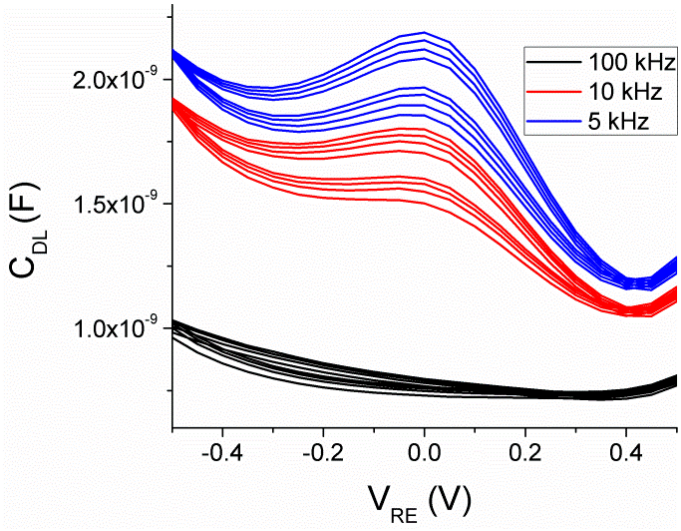

Figure 2.7 CV experiments, measured from a on a 100µm x 100µm Au electrode to a reference Ag/AgCl electrode. Shown is 100mM $MgCl_2$. Swept 4 times both ascending and descending in bias voltage, the average capacitance of each sweep was taken and fitted to the f^{α} model for the impedance spectroscopy fit. Best fit for this experiment was α = -.51.

2.3.3 Results

For the extraction algorithm of section 2.3.2, the results of Table 2-1 were found for varying salinities of an $MgCl_2$ and NaCl mixed polyelectrolyte solution.

Table 2-1 Circuit parameters extracted for 20μL of 1mM NaCl added to 20μL of the solution in column 1.

Parameter	R_{sol} (kΩ)	$C_{DL\text{-}avg}$ (μF/cm^2)
De-Ionized Water	42 ± 55%	2.0
1 μM $MgCl_2$	42 ± 51%	2.0
10 μM $MgCl_2$	41 ± 47%	2.0
100 μM $MgCl_2$	40 ± 42%	2.1
1 mM $MgCl_2$	20 ± 41%	4.6
10 mM $MgCl_2$	4.5 ± 38%	10.2
100 mM $MgCl_2$	1.2 ± 36%	19.2

While the extracted parameters yield values encompassing what would be expected from theoretical calculations and other works [5], the error margins are very high. This makes clear that a more comprehensive model is needed for experimental analysis, let alone device design.

CHAPTER 3

THE IONIC DRIFT-DIFFUSION TRANSPORT CLOSE TO THE STERIC LIMIT

3.1 Abstract

Modeling of the distribution and motion of ions in an electrolyte near a charged solid surface is critical for building the interface between electronics and chemical/biological functions. To account for the dynamics of the steric hindrance, the size-modified Poisson-Boltzmann model has to be solved self-consistently with the proper transport formalism to describe the transition from the dilute buffer to the densely packed layer. In this work, we start from the mean-free path collision theory to derive how the diffusivity should decrease towards the steric limit, and then formulate the associated Einstein relation in view of detailed balance. We illustrate our new ionic transport model of drift-diffusion with numerical simulation in COMSOL, and present a simple transient experiment for model verification and parameter extraction.

3.2 Introduction

Electronic interface to the chemicals and molecules in an electrolyte has many biological, biomedical and environmental applications, but the dynamic response to complex stimulation still lacks of predictive models to describe the ionic transport that account for the steric ion size effect [1]. It has become clear that when the solid-electrolyte surface potential is greater than a few kT, the surface concentration will be

limited by the hydrated ionic size due to steric hindrance and the quasi-static net charge will be corrected by the size-modified Poisson-Boltzmann (SMPB) model [11, 12, 34]:

$$\nabla^2\varphi = -\frac{q}{\varepsilon}\sum_i z_i n_i = -\frac{q}{\varepsilon}\sum_i \frac{z_i n_{i0}\exp\left(-\frac{z_i\varphi}{V_T}\right)}{1+\sum_j a_j^3 n_{j0}\exp\left(-\frac{z_j\varphi}{V_T}\right)} \qquad (3.1)$$

where ϕ is the electrostatic potential, q is the elemental charge, ε is the dielectric constant of the buffer, and V_T is the thermal voltage. For the i-th ion, z_i, n_i, n_{i0} and a_i are the valency, local concentration, bulk concentration and effective size, respectively. The local ion concentration will be close to the Boltzmann distribution in the dilute approximation and capped by $1/a_i^3$ in the steric limit [12]. The ordered ionic packing in the steric limit had been experimentally observed recently [35, 36]. As an illustration, for a 100mM NaCl mono-electrolyte with the reference electrode at the right boundary and the non-amperometric surface (such as a polarizable electrode, SiO_2 or Ta_2O_5) at the left boundary, the net charge ρ and the potential ϕ predicted by SMPB are shown in Figure 3.1 for surface potentials changing from –500mV to 500mV.

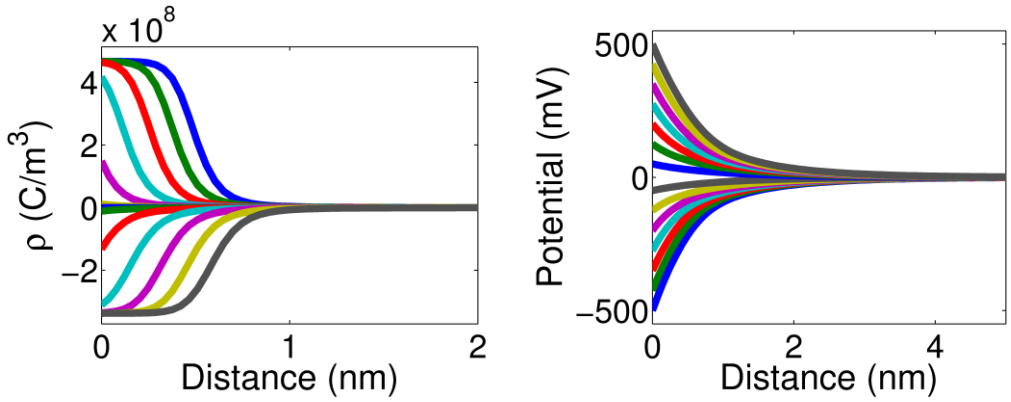

Figure 3.1 (Left) SMPB prediction of net charge profiles of ions extending from a charged non-faradaic electrode (x = 0nm) to a grounded bulk solution of 100mM NaCl with a_{Cl^-} = 7.8Å and a_{Na^+} = 7.0Å. The surface potentials vary from 500mV (lowest curves) to -500mV (highest curve) in 67mV steps. The slightly higher ionic size of a_{Cl^-} establishes a lower maximum interface concentration at positive surface potentials. (Right) Corresponding electrostatic potential profiles.

3.3 Mean Free Path from the Ideal Gas Theory

We start the ionic transport model from the drift-diffusion formalism in an ideal gas theory. For a polyelectrolyte with k types of ions, the i-th ion will have the mean free path l_i between ion collisions as,

$$l_i = \frac{1}{\sum_{j=1}^{k} \sigma_{ij} n_j} \qquad (3.2)$$

where σ_{ij} is the collision cross section between the *i*-th and *j*-th ionic species. In the first-order approximation, we can estimate σ_{ij} by the effective size of the *i*-th and *j*-th molecules:

$$\sigma_{ij} = a_i a_j \qquad (3.3)$$

In polyelectrolytes, there are two kinds of collisions: background collision with the vibrating water molecule and collision with other ionic species. Following the Matthissen's rule, the diffusivity of the *i*-th ion in the polyelectrolyte can be expressed as:

$$\begin{aligned} D_i = v_{thi} l_i &= v_{thi} \left[\left(\frac{1}{\sum_j \sigma_{ij} n_j} \right)^{-1} + \left(\frac{1}{\sigma_{io} n_o} \right)^{-1} \right]^{-1} \\ &= v_{thi} \frac{1}{a_i \sum_j a_j n_j + \sigma_{i0} n_0} \end{aligned} \qquad (3.4)$$

where v_{thi} is the thermal velocity [37] of the *i*-th ions, which depends on $\sqrt{T / m_i^*}$ with T being the ambient temperature and m_i^* the effective hydrated mass of the *i*-th ion. The term σ_{i0} represents the collision cross section between the *i*-th ion and the vibrating water molecule and n_0 is the effective density of the vibrating water molecule. Similar to the scattering integral in crystals, n_0 is an extracted parameter and is expected to be much smaller than the actual water molecule density due to the principle of indistinguishable particles.

At the dilute approximation, we have $a_i \sum_j a_j n_j << \sigma_{i0} n_0$ and $\sum_j a_j^3 n_j << 1$, i.e., the diffusivity is dominated by collision with vibrating water molecules and we are far from the steric limit. Thus we can define the ionic diffusivity in the dilute approximation as:

$$D_{i0} = v_{thi} l_{i0} = \frac{v_{thi}}{\sigma_{i0} n_0} \qquad (3.5)$$

where l_{i0} and D_{io} are the mean free path and the diffusivity for the i-th ion in the dilute approximation, respectively. We hence obtain the ebbed diffusivity correction close to the steric layer:

$$\begin{aligned} D_i &= v_{thi} \frac{1}{a_i \sum_j a_j n_j + \sigma_{i0} n_0} \\ &= \frac{v_{thi}}{\sigma_{i0} n_0} \cdot \frac{1}{\left(1 + \frac{a_i \sum_j a_j n_j}{\sigma_{i0} n_0} \right)} = D_{i0} \frac{1}{1 + A_{i0} \sum_j a_j n_j} \end{aligned} \qquad (3.6)$$

where $A_{i0} \equiv l_{io} a_i$ is the free-motion trajectory area of the i-th ion under dilute approximation. As usually $l_{io} >> a_i$ and $A_{io} >> a_i^2$, in the steric limit of one dominant ion at the surface,

$$\lim_{n_i \to 1/a_i^3} \frac{1}{1 + A_{i0} a_i n_i} << 1 \qquad (3.7)$$

The diffusion mechanism in the densely packed layer is often swapping assisted by interstitials, which is not considered in the collision theory above. Thus, at the steric limit when the hydrated ions are densely packed, the diffusivity by the swapping

mechanism, denoted as D_S, represents an independent mechanism, and hence we can add the swapping and collision mechanisms together when the steric limit is approached:

$$D_i = D_{i0} \frac{1}{1 + A_{i0} \sum_j a_j n_j} + D_S \cdot \left(\sum_j a_j^3 n_j \right) \qquad (3.8)$$

Although Eq. 3.8 has the correct asymptotic trends in both dilute and steric limits, there are a few physical effects that we have ignored.

- Collision is assumed to entirely randomize the ionic motion, and ions are considered spherical.
- Eq. (3.3) is a rough estimate for the collision cross section, ignoring the detailed repulsive and attractive potentials. In the steric limit, the repulsive potential is only reflected in the effective hydrated ion size a_i.
- The steric layer may have complicated composition due to de-screening [38] and charge reversal [39]. Our model will converge to SMPB in the steady state, and have similar limitations on the steric layer composition.

In the classical derivation of the Einstein relation between diffusivity and mobility under the dilute approximation, we have:

$$\mu = \frac{ql}{m^* v_{th}} = D \frac{q}{m^* v_{th}^2} = D \frac{q}{kT} \qquad (3.9)$$

where μ is the mobility in cm^2/Vs. If we consider the DD transport of the charged i–th ion with positive charge of qz_i,

$$J_i = J_{drift,i} + J_{diff,i} = qz_i\left(\mu_i n_i F - D_i \nabla n_i\right) \qquad (3.10)$$

where for the *i*-th ion J_i is the ionic flux, $J_{drift,i}$ is the drift flux by the local electric field F, $J_{diff,i}$ is the diffusion flux by concentration gradient. Under the detailed balance condition in equilibrium in 1D,

$$J_i \equiv 0; \quad \Rightarrow \quad \mu_i n_i F = D_i \frac{dn_i}{dx} \qquad (3.11)$$

When there are space charges and built-in electric fields (i.e., $F \neq 0$), we can solve Eq. (3.11) as:

$$n_i(x) = n_i(x_0) \cdot \exp\left(\int_{x_0}^{x} \frac{\mu F(x')}{D} dx'\right) \qquad (3.12)$$

If the classical Einstein relation in Eq. (3.9) holds under the dilute approximation, the exponential relation in Eq. (3.12) can lead to unphysically large ionic concentration under large surface potential. The Einstein relation has to be properly modified when n_i is capped by a_i^{-3}, similar to the density-of-state consideration in the degenerate carrier concentration in semiconductors [40]. Steric repulsion is required to stabilize the ionic model system by eliminating unrealistic boundary layers. From Eq. (3.12), in the steric layer when only one molecule is present, the saturated ionic concentration is only possible when

$$\lim_{n_i \to 1/a_i^3} \frac{\mu_i}{D_i} \to 0 \qquad (3.13)$$

In other words, in the DD transport formalism, the steric limit of ionic concentration is set by the condition when the ratio of mobility and diffusivity goes to 0. We will take a linear approximation for the Einstein relation in the steric limit:

$$\frac{\mu_i}{D_i} = \frac{q}{kT}\left(1 - \sum_j a_j^3 n_j\right) \qquad (3.14)$$

If we consider the mobility explicitly expanded from Eq. (3.8), we then have:

$$\mu_i = \frac{qD_{i0}}{kT} \cdot \frac{1 - \sum_j a_j^3 n_j}{1 + A_{i0} \sum_j a_j n_j} + \frac{qD_S}{kT} \cdot \left(\sum_j a_j^3 n_j\right)\left(1 - \sum_j a_j^3 n_j\right) \qquad (3.15)$$

Notice that at the steric limit, $\mu_i = 0$, $F \neq 0$, and $D_i \neq 0$, but $J_{diff,i} \to 0$ due to $\frac{dn_i}{dx} \to 0$, and hence the zero flux condition for equilibrium can be established.

For a non-faradaic contact, the drift and diffusion terms must cancel in the steady state to give no change in concentration with respect to time for any of the ionic species in solution. Using the electrostatic potential and ionic concentrations as the basic variables, the complete DD ionic transport formalism for the *i*-th ion with positive z_i can thus be summarized in the Poisson and continuity equations:

$$\nabla^2 \varphi = -\frac{q}{\varepsilon} \frac{\sum_i z_i n_i}{1 + \sum_i a_i^3 n_i} \qquad (3.16)$$

$$\frac{\partial n_i}{\partial t} = \nabla \cdot \left(q z_i \left(\mu_i n_i F - D_i \nabla n_i\right)\right) \qquad (3.17)$$

where D_i and μ_i are given in Eqs. (3.8) and (3.15), respectively.

3.4 Implementation and Parameter Extraction

We implement the above drift-diffusion model in COMSOL to observe the effects of the mobility and diffusivity corrections. For the diffusivity in the dilute limit, we have used parameters from the literature around 1.5×10^{-5} cm^2/s [40, 41]. This parameter can also be extracted from the conductivity in a low-salinity solution. We have chosen a_{Na} and a_{Cl} as 0.70 nm and 0.78 nm for now to be consistent with those in SMPB of Figure 3.1. Alternatively one can use a value derived from a hydration or coordination number [27]. Notice that the ionic effective sizes derived from steric models tend to differ from the hydrated ion size in bulk solutions significantly [42]. The mean free path is related to the thermal velocity and the hydrated mass shown in Eq. (3.4) and is set at $50a_i$ for illustration. We choose a mean free path significantly larger than a_i to highlight the model. As shown in Figure 3.2(a – c), when the surface potential and the bulk salinity are high, both mobility and diffusivity decrease towards the steric limit, but the relative rate of the mobility reduction with respect to concentration is required to be higher than that of the diffusivity, which is the criterion for the steric layer to form in the drift-diffusion model by Eq. (3.13).

In Figure 3.2(d), we show a simulation study to highlight the steric limit setup in the new formalism. A 300mV surface potential is applied and the system is allowed to relax to the steady state in three scenarios: (1) Both SMPB of Eq. (3.16) and DD of Eq. (3.17) use the same $a_i = a_{i0} = 0.70$nm; (2) DD uses $a_i = 0.35$nm and SMPB uses $a_i = 0.70$nm; (3) SMPB uses $a_i = 0.35$nm and DD uses $a_i = 0.70$nm. It can be derived

that the steady-state maximum steric concentration is set by the Einstein relation in Eq. (3.13) instead of SMPB when the ionic transport is modeled by Eqs. (3.8) and (3.15) – (3.17). This is because the drift and diffusion fluxes have to be exactly balanced out to reach steady state with a non-amperometric boundary, which can only happen when $\mu/D \to 0$ in the steric layer.

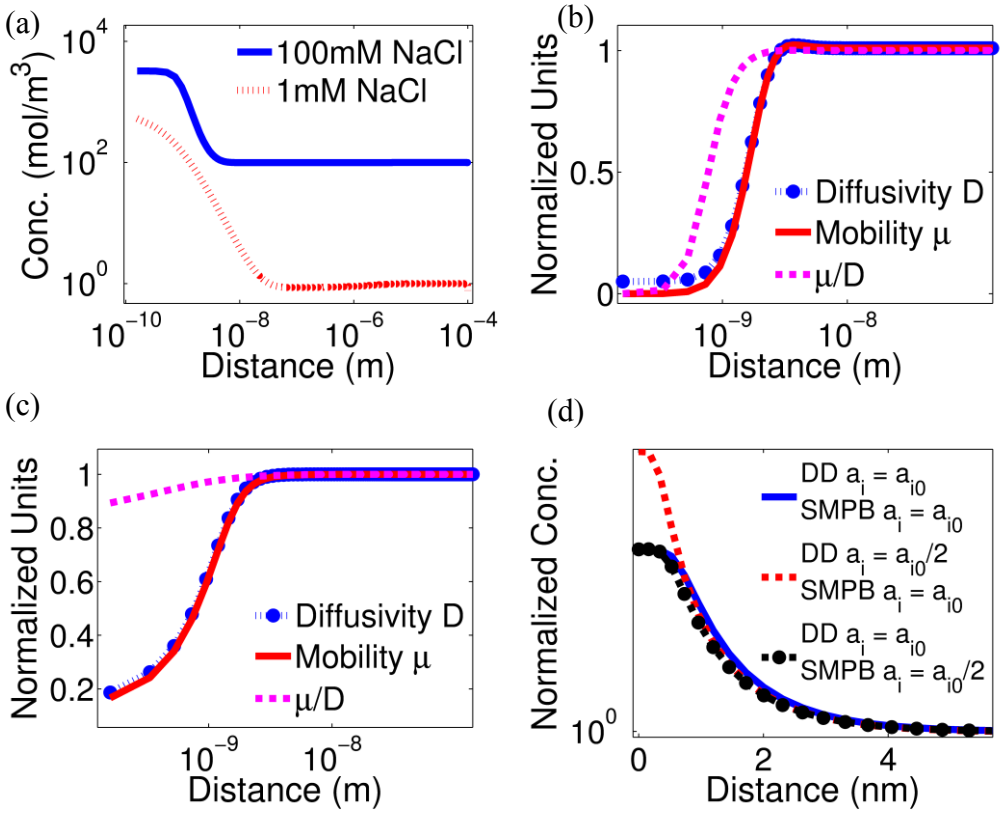

Figure 3.2 (a) Concentration profiles for two molarities of NaCl, showing a steric layer forming for the 100mM but not 1mM NaCl. Mobility and Diffusivity versus distance with surface potential at 300mV for: (b) 100mM NaCl and (c) 1mM NaCl. (d) Concentration of Na+ vs. distance for steady state solution after 300mV step for variation of ai in the SMPB and DD portions of the simulation. Lowering

the DD ai in Eq. (3.17) will adjust the interface concentration, while lowering the SMPB ai in Eq. (3.16) does not, indicating that the Einstein relation in Eq. (3.13) is the critical modification to set the steric hindrance maximum.

Direct electrical observation of the steric effect is difficult due to large noise in transient IV curves, and the small size of a_i and the condensed layer. While atomic force microscopy has given insight into the structure and packing topology [35], it does not offer insight into the dynamic features. However, since a_i determines at what surface potential the condensed layer begins to form [4], by stepping the potential difference between the electrolyte and the surface, we may observe a change in the transient response corresponding to the onset of the condensed layer. This will manifest itself as both a change in the differential capacitance (which is also manifest in SMPB), and a deviation from a single-time-constant exponential decay in the step response. This transient feature results from a concentration-dependent mobility, and thus can be used to both extract a_i and validate the proposed transport model. At low biases, the transient current response will be dominated by a single time constant, while at higher biases, the decreasing mobility in the condensed layer will cause the current response to extend much longer than the exponential tail described by a single time constant.

By delivering a series of pulse steps to 100mM NaCl from 50mV to 300mV in 10mV steps and comparing the transient current to a single-time-constant exponential decay predicted by the Poisson-Boltzmann model (i.e. the Debye approximation), an estimate of a_i can be made. Also as the first few IV points can be very noisy, a

Savitsky-Golay filter was applied before fitting, as shown in Figure 3.3. From both positive and negative pulses, we extract a_{Na} and a_{Cl} as .70± .11 nm and .78±.13 nm, respectively. We further show the intrinsic J_{diff} and J_{drift} transient for Na^+ during the step bias in the inset of Figure 3.3(d), as well as the corresponding Na^+ concentration and electrostatic potential, in Figure 3.3(e,f). Here we can observe the detailed dynamic features of the intrinsic variables $\varphi(t)$ and $n_i(t)$ during a step surface potential, which offer much more insight during the transition than just the SMPB model.

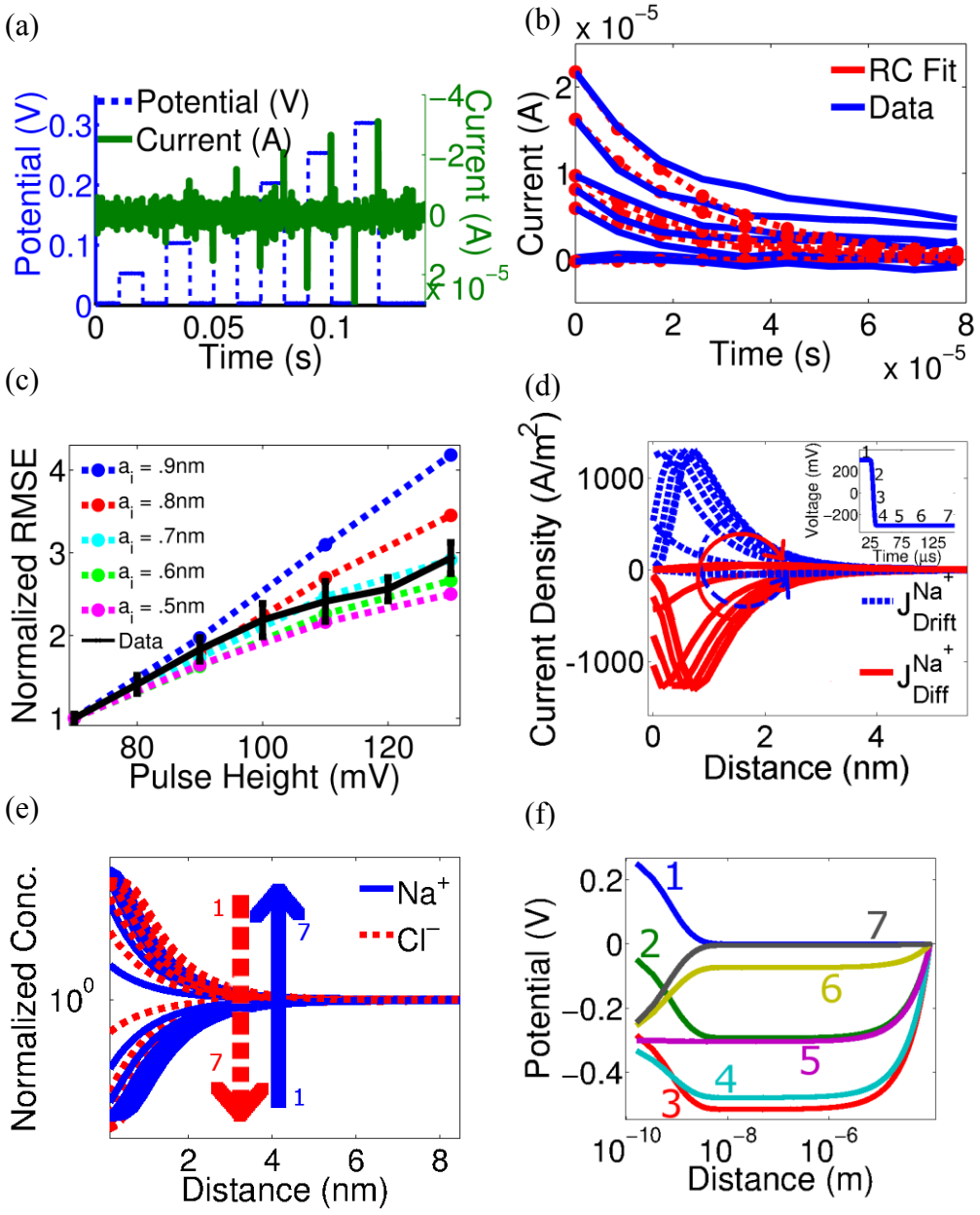

Figure 3.3 (a) Staircase bias experiments of 100mM NaCl with pulses in 50mV increments from 50mV to 300mV. (b) Filtered transient current of each pulse overlaid, with single time constant fitting. Significant deviation from exponential occurs between 100 and 150mV. (c) COMSOL staircase bias simulation from 70-130mV with normalized root-mean-square error (RMSE) of exponential fitting versus pulse height. As the pulse height increases, the steric effects begin to cause

the current response to deviate from a single-time-constant response. Experimental data of 100mM NaCl indicate Na^+ effective ionic size can be best fit by a_i = 0.70nm. (d) Current density vs. distance for the drift and diffusive fluxes of the Na^+ ion transport during the bias step from 300mV to -300mV. The curved arrows indicate the progression of the current density for time steps 2-7 in the inset. (e) Transient concentration profiles and (f) Transient potential profiles for time steps 1-7.

3.5 Conclusion

We have presented a new ionic transport formalism based on drift-diffusion with modified diffusivity and Einstein relation to transition smoothly between the dilute and steric limits. The condition for this model to approach SMPB in the steady state is identified. Transient features, particularly the ebbed diffusivity and mobility towards the condensed layer, have been examined by COMSOL simulation. We then present a simple experiment for model validation and parameter extraction. The new model can give new insights to the design of electronic interface to electrolyte, as well as serve as the base to investigate the dynamics of polyelectrolytes.

CHAPTER 4

STERIC POLYELECTROLYTE EBBED DRIFT-DIFFUSION

4.1 Abstract

To account for the steric effects near the electrolytic-solid interface, we have discovered modifications required to the classical Einstein relationship between mobility and diffusivity in densely packed regions under high electric fields. After initial description and validation with mono-electrolytes, we turn to investigating the numerical implementation and physical characteristics of the more complex polyelectrolytes. The numerical property actually lend intuition to the physical rigor and consistency of the model. Analysis of the polyelectrolyte behavior close to the steric limit and shows insight into the ionic distribution effects at biological sensor interfaces.

4.2 Introduction

Understanding the precise nature of the interface between a solid surface and saline solution has become of increasing interest with the advent of field-effect sensing [17, 43-46]. Based on the steric hindrance effect for the electrical double layer (EDL) [11, 12, 47], the Einstein relation between mobility and diffusivity was modified to account for the dynamics of high concentration effects as described in chapter 3. The transient

response to complex stimulation in realistic polyelectrolytes requires physical finite-element models for the solid-liquid interface in order to account for effects from electrode geometry and ionic profiles [1]. However, previous models of the steric repulsion and ion correlation at the solid-liquid interface was mostly restricted to quasi-static description without consideration of the dynamic interaction of the EDL to the dilute buffer [12]. Furthermore, the EDL composition may depend on surface potential, ionic species and salinity [16, 35], before electrical stimulation has even been taken into account. Present dynamic models of this interface range in complexity from lumped circuit models, which do not capture the distributive effects of the solution, to full molecular dynamics simulations [45], which are still too computationally expensive for device design and provide limited intuition. As a comprehensive but computationally tenable simulation tool for that can capture the dynamic effects of steric repulsion and ion correlation, we expand the steric hindrance model to a new steric polyelectrolyte ebbed drift-diffusion (SPEEDD) model for transient EDL behavior with respect to ionic species, bulk concentration, electrode geometry and surface potentials larger than kT. We examine the new predictions of the polyelectrolyte composition from the model, and analyze the numerical properties such as gridding and convergence for further insight and verification.

4.3 Size Modified Poisson-Boltzmann Equations for Polyelectrolytes

The mathematical description of charge and potential profiles for a mean-field description of the interface between a solid surface and electrolyte solution has seen

significant refinement over the past 150 years. From Helmholtz's initial description [6], Gouy and Chapman's double layer explanation [22, 48], Stern's refinement [33], Grahame's extensive experimental additions [49], we now describe the interface using a Size-Modified Poisson-Boltzmann (SMPB) formalism to explain the complex relaxation of the electric field at the electrode-electrolyte interface including the steric repulsion [11, 12, 42].

$$\nabla^2\varphi = -\frac{q}{\varepsilon}\sum_i z_i n_i = -\frac{q}{\varepsilon}\sum_i \frac{z_i n_{i0}\exp\left(-\frac{z_i\varphi}{V_T}\right)}{1+\sum_j a_j^3 n_{j0}\exp\left(-\frac{z_j\varphi}{V_T}\right)} \qquad (\ 4.1\ )$$

Where φ is the electrostatic potential, q is the elemental charge, ε is the dielectric constant of the buffer, V_T is the thermal voltage, and z_i, n_i, n_{i0} and a_i are the valency, local concentration, bulk concentration and effective size for the i-th ion, respectively. This approach blends the utility of a mean-field description, with accuracy for both capacitance and charge profile predictions at high (more than a few kT) interfacial potentials.

The underlying assumption of SMPB models is that the interface is at steady state. For a 1:1 electrolyte (e.g. 10mM NaCl with an electrode feature size ~100μm) the equilibration time is on the order of tenths of microseconds for the steric layer, and tens-hundreds of microseconds for the diffuse layer [12, 50, 51]. Expanding a Poisson-Nernst-Planck approach to a 1:1 electrolyte with size modification [47] gives mathematical insight into the processes that are expected to occur as the time scales of electrical perturbations decrease below the double layer relaxation times, however an

electrolyte solution with multiple ionic species requires a numerical approach. Coupling of Drift-Diffusion (DD) equations with an SMPB model (where concentrations are not assumed to be exponential), allows for the analysis of more complex electrolytes.

$$\nabla^2\varphi = -\frac{q}{\varepsilon}\frac{\sum_i z_i n_i}{1+\sum_i a_i^3 n_i} \qquad (4.2)$$

$$\frac{\partial n_i}{\partial t} - R_i = \nabla\cdot\left(q\mu_i n_i \nabla\varphi + qD_i\nabla n_i\right) = \nabla\cdot J_i \qquad (4.3)$$

Eq (4.3) represents the continuity conditions with mobility and diffusivity controlling transport as μ_i and D_i, where R_i represenents any bulk ion concentration change. In steady state, an electrolyte system with a polarizable electrode on at least one side will have both Eq. (4.3) and J_i asymptotically trend to zero. The modified forms of μ_i and D_i are:

$$D_i = D_{i0}\frac{1}{1+A_{i0}\sum_j a_j n_j} + D_S\cdot\left(\sum_j a_j^3 n_j\right) \qquad (4.4)$$

$$\frac{\mu_i}{D_i} = \frac{q}{kT}\left(1-\sum_j a_j^3 n_j\right) \qquad (4.5)$$

where D_{i0} is the bulk diffusivity, A_{i0} is the free-motion trajectory area of the i-th ion under dilute approximation, and D_s is the diffusivity association with swapping in the densely packed layer.

4.4 Gridding and Stability

The steric layer is on the order of nanometers, and the voltage decay into solution varies from nanometers to a tenth of a micron by the scale of the Debye length which depends on salinity. Full recovery to bulk concentration may be on the micron scale [5].

To deal with these length scales in a reasonable computation time, it is best to employ an inhomogeneous discretization, with short distance steps near the polarizable electrodes when the surface potential changes rapidly, and longer ones near the bulk of the solution with smooth potential and concentration profiles. Homogeneous gridding is either too coarse for an accurate solution near the interface, or too computationally unwieldy (in both computation time and memory requirements) to be a viable option, especially in 2D and 3D cases.

Two options are available in the COMSOL suite to address this issue. One is, given an approximate solution to the problem (the exponential solution of the Debye-Hückel model [52]), a discretization following a geometric progression can be applied to give an exponential change in element size over the model domain. Another option is to apply the adaptive mesh refinement system implemented in COMSOL. Adaptive mesh refinements operate by locating the areas of largest residual error in the simulation, and refining the mesh in those areas until a certain tolerance is reached [53, 54]. While adaptive mesh refinement will lead to guaranteed lower bound, it requires multiple iterations of solving to complete the algorithm, and so trades computational time for accuracy [55]. For a trade-off in accuracy and computational time in a situation where

areas of the most and least rapid changes are known, the best solution is to start from an explicitly inhomogeneous discretization, and run a few iterations of an adaptive mesh refinement to minimize error.

Boundary conditions of the model determine the characteristics of the electrodes including potential (φ), ionic concentration (c_i) and fluxes (J_i). A zero-flux condition for all species indicates a non-faradaic electrode, where, while ions may pile up near the boundary causing a transient current, there will be no transfer of ionic species across the boundary. This is also called the polarizable electrode. A large reference electrode operating as the intended function of pinning the electrochemical potential (not reaction limited), can be simulated by setting a constant concentration for the ionic species which can be transferred across the boundary (i.e. Cl^- in an Ag/AgCl setup with a Cl based electrolyte), and establishing a zero-flux constraint for all other ionic species. Specifying Dirichlet boundary conditions for potential for each electrode completes the 1D description for the partial differential equations, and adding Neumann boundary conditions for boundaries other than electrode edges in 2D and 3D systems creates a well-conditioned model. To explore the differences between simple and complex saline solutions' steric layer dynamics, we examine a system of various solutions exposed to a 300mV bipolar pulses. This allows the examination of the formation and dissipation of both cationic and anionic steric layers. The differences in transient simulation between the polarizable (non-faradaic) and non-polarizable (faradaic reference electrode) are shown in Figure 4.1.

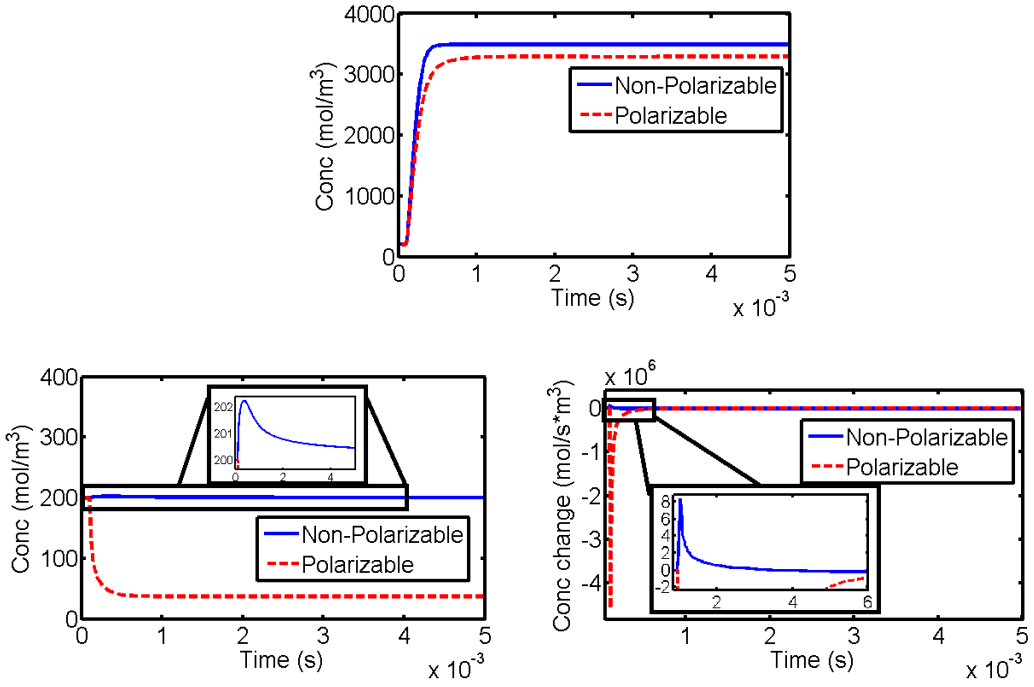

Figure 4.1 Simulation results for polarizable and non-polarizable electrode boundary conditions, stimulated by a -300mV pulse for a 100mM NaCl and 50mM $MgCl_2$ mixture. (Top) Interface concentrations at the grounded, polarizable electrode, showing Cl^- ions piling up at the surface. (Bottom Left) Concentration at the driving electrode. The polarizable electrode shows decrease in concentration, while the non-polarizable electrode shows a slight increase in concentration indicating a flux of Cl^- ions into the solution. (Bottom Right) Time derivative of concentration near the driving electrode.

The small bumps in the concentration at the driving non-polarizable electrode indicates the flux of ions through the interface which allows for a return to bulk. The polarizable electrode, lacking this mechanism, does not have a return to bulk, and thus has a concentration gradient through the solution.

With the coupled differential equations having multiple parameters depending on the coupled variables, all parameters must be reassessed for additional dependencies. The treatment of maximum ionic concentrations near a surface on ionic transport properties, such as diffusivity and mobility examined previously in chapter 3, has a strong effect on the overall numerical stability of SPEEDD. In particular, to correctly account for the balance between drift and diffusion current components required for a steady-state concentration solution throughout the electrolyte regions, the Einstein relation of the mobility and diffusivity will correspond to the maximum number of ions close to the surface. When:

$$\sum_j a_j^3 n_j \to 1 \quad , \quad \frac{\mu_i}{D_i} \to 0 \qquad (4.6)$$

We can see that SPEEDD has implemented this modified Einstein relation in Eqs. (4.4, 4.5) in the first-order approximation. The physical meaning is that the Steric layer has ebbed diffusivity according to Eq. (4.4), but the mobility has to reduce even faster when the concentration becomes saturated due to steric repulsion, i.e., the randomized ion motion is reduced in the maximum concentration of the steric layer when the concentration gradient becomes small, but the drift term has to diminish accordingly in this region with large field gradient by a sharper reduction in mobility. Without the proper correction on the Einstein relation, i.e., when diffusion cannot balance out drift in the steric layer, a solution will not converge unless the first discretization is significantly greater than a_i of the largest co-ion, as shown in Figure 4.2.

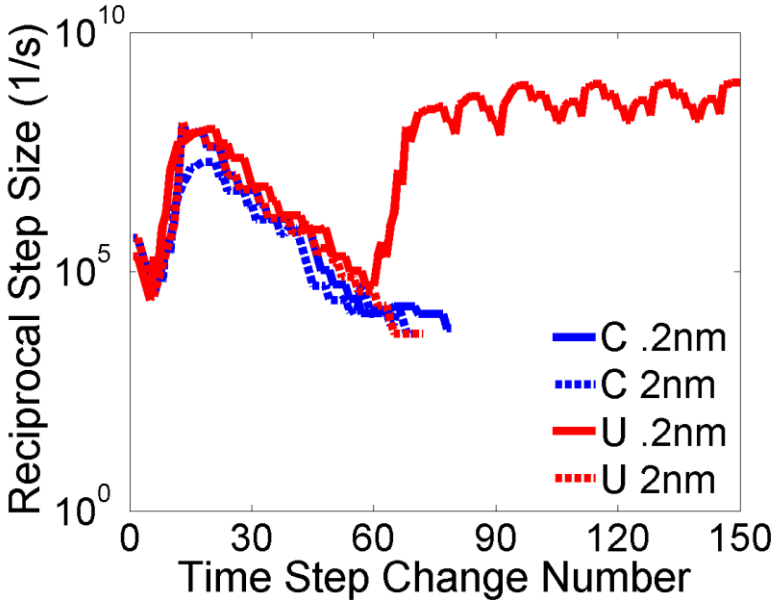

Figure 4.2 Convergence properties of modified (M) and constant or uncorrected (U) Einstein relations for a 300mV step for 2nm and .2nm discretization near the interface. For 2nm discretization with $a_i \sim .7$nm, both the corrected and constant Einstein relation simulations converge to similar solutions, however for the .2nm discretization, the constant Einstein relation fails to converge (oscillating solid red curve continues to oscillate until an exception is thrown), while the corrected system yields the same solution but with a finer mesh. The time step change number indicates each time during the course of the solution that the time step had to be adapted.

4.5 Parametric Variations

4.5.1 a_i - The effect of the Steric parameter

The ionic size parameter, a_i will determine the potential at which the Steric effects begin to come into play, as well as the maximum interface concentration. Larger a_i equate to a lower maximum concentration for the Steric layer, and thus a lower φ at which this concentration is reached. An example of the effect of varying ionic size on the condensed layer is shown in Figure 4.3.

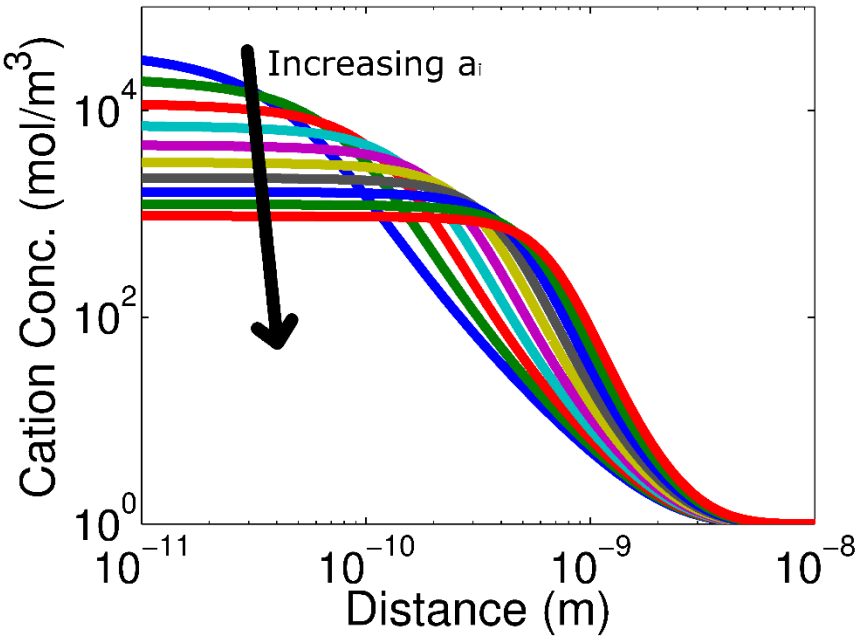

Figure 4.3 Effect of varying a_{Mg} 3Å to 12Å, from COMSOL simulation. As a_{Mg} increases, the maximum concentration possible at the interface decreases, and the Steric layer extends further into solution. Bulk concentration is 100mM = 100 mol/m^3, and φ=300mV at the interface x = 0m.

As a_i increases, the maximum interface concentration decreases. The electric field must still be compensated, however, and thus the steric layer extends further into the solution. Concerning net current predictions, the primary effect of varying the ionic size is the influence the magnitude of the current, as shown in Figure 4.4.

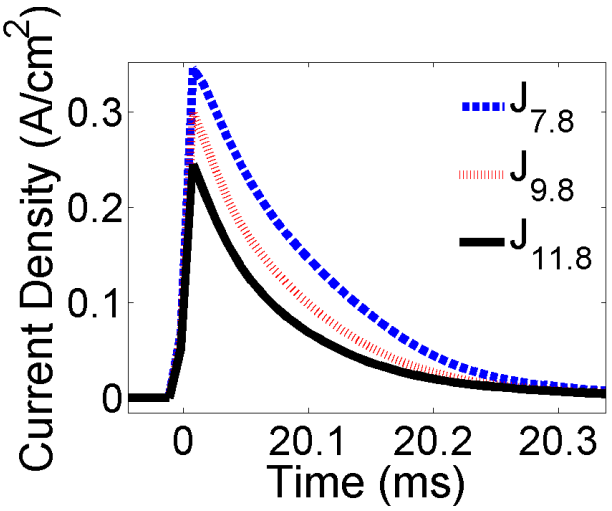

Figure 4.4 Effect of varying a_{Mg} between 7.8Å, 9.8Å, and 11.8Å. As a_{Mg} increases, the net current seen through the solution decreases.

A decrease in a_i thus increases not only increases the steric limit on the interface concentration, but the transient current as well. This is expected as a higher number of ions must move away from the interface.

4.5.2 The Effect of Ebbed Diffusivity on Transient Ion Concentration

The modified Einstein relation has the same effect in the dynamic SPEEDD model as the steric correction for the static solution in the SMPB model, which will prevent unphysically high concentrations, as shown in Figure 4.5. The solution with revised

Einstein relation reaches a steady state on the order of microseconds, while the uncorrected concentration continues to rise to unphysical concentration levels on a too long a time scale. This is expected as while the SMPB alone would limit the interface concentration, the coupling with the drift and diffusion currents do not cancel without the mobility and diffusivity correction, leading to the unphysical interface concentration prediction.

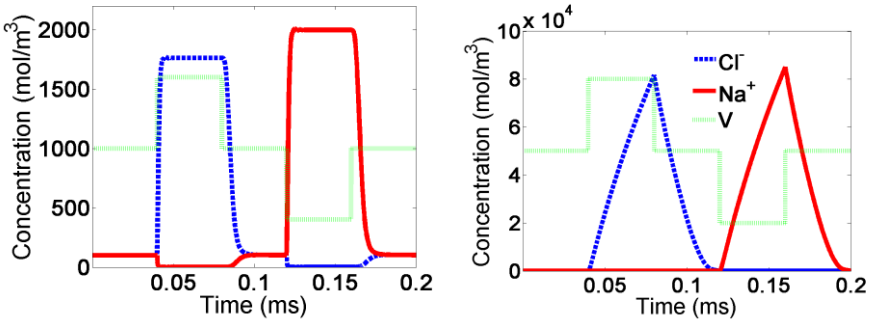

Figure 4.5 Interface concentrations (at the first grid-point 2nm from the interface) of the modified Einstein relation (left) and the constant or uncorrected Einstein relation (right) solutions to bipolar 400µs, 300mV bipolar pulses applied to 100 mol/m^3 NaCl. The mobility corrected solution reaches a steady state on the order of microseconds, while the uncorrected concentration continues to rise to unphysical concentration levels on a too long a time scale.

4.5.3 Approximations in a mono-electrolyte

Applying the SPEEDD model to a saline solution where only Na^+, Cl^-, and water molecules (i.e. not a molten salt) are in the electrolyte, approximations can be made to create a more intuitive understanding of the factors at play in the model. Under a

negative surface potential (treating the bulk solution as ground) at the non-Faradaic electrode, Eq. 3.8 can be simplified to:

$$D_{Na} = D_{Na0}\frac{1-a_{Na}^3 n_{Na}}{1+A_{Na}a_{Na}n_{Na}} \qquad (\ 4.7\ )$$

$$D_{Na} = D_{Na0}\frac{1-a_{Na}^3 n_{Na}}{\left(1+\left(A_{Na}a_{Na}n_{Na}\right)^m\right)^{1/m}} \qquad (\ 4.8\ )$$

Note that close to the Steric layer, $n_{Cl} << n_{Na}$ under such surface potential so that we can simplify the summation term in Eq 3.8. We have only applied the Caughey-Thomas fitting to the denominator, instead of the numerator in Eq. 4.8, because the denominator deals with the transition from dilute to semi-Steric approximations (comparing $A_{Na}a_{Na}$ to n_{Na}) while the numerator deals with the transition from semi-Steric to solid lattice approximations (comparing $a^3{}_{Na}$ and n_{Na}). Table 4-1 examines how the numerator and denominator in Eq. 4.8 contribute to the ebbed diffusivity by assuming $A = l{\cdot}a = 50a^2$ when n approaches the Steric limit of $1/a^3$.

Table 4-1 Decreasing rate of diffusivity by different terms in Eq. 4.8 with $A = l{\cdot}a = 50a^2$

$\frac{n}{\left(\frac{1}{a^3}\right)}$	$1-a^3n$	$\frac{1}{1+Aan}=\frac{1}{1+50a^3n}$	$\frac{1}{\left(1+\left(Aan\right)^2\right)^{0.5}}=\frac{1}{\left(1+\left(50a^3n\right)^2\right)^{0.5}}$
0.001	0.999	0.95	0.999
0.01	0.99	0.66	0.89

0.1	0.9	0.17	0.20
0.2	0.8	0.091	0.10
0.25	0.75	0.074	0.080
0.5	0.5	0.038	0.040
0.75	0.25	0.026	0.027
0.9	0.1	0.022	0.022
1	0	0.020	0.020

It is clear that the denominator $\frac{1}{1+Aan}$ is more critical for $0.001 < a^3n < 0.5$, and the numerator $(1 - a^3n)$ becomes dominant after $a^3n > 0.75$, when the denominator stops changing around 0.02. For $m = 2$ in the Caughey-Thomas approximation, the main difference is for small values of a^3n, between 0.001 and 0.1, or as the concentration is significantly less than the Steric limit.

For this analysis the solid diffusion part of Eq. 3.8. has been excluded for simplicity. The effect of D_S at the Steric limit can be appended in a straightforward manner. For complete dynamic modeling of all ions, the modified Poisson equation and the drift diffusion equation will be:

$$\nabla^2\phi = -\frac{q}{\varepsilon}\frac{\sum_i z_i n_i}{1+\sum_i a_i^3 n_i}, \text{ where } i = Na^+ \text{ and } Cl^- \qquad (4.9)$$

$$\frac{\partial n_i}{\partial t} = \nabla \cdot qD_i \left(\frac{z_i n_i}{V_T} \nabla \phi + \nabla n_i \right) \qquad (4.10)$$

From the transient IV waveforms of gathering and dispensing the Na^+ Steric layer, the material parameters of D_{Na0}, a_{Na}, and A_{Na} can be extracted. The similar parameter set will be needed for Cl^-. The basic dependent variables are ϕ, n_{Na} and n_{Cl}. The methods for this extraction are covered in the following section.

As Eq. 4.10. contains second-order spatial derivatives, the steady state solution will need at least one Dirichlet (specifying a dependent variable value at the boundary) and one Neumann (specifying the value of a dependent variable's derivative) boundary conditions. Two Dirichlet boundary conditions at the two sides of the 1D problem will yield a well-conditioned numerical system. The transient solution has the time derivative only at the first order (as a parabolic partial differential equation system), so if the initial conditions of ϕ, n_{Na} and n_{Cl} are given for all spatial points at $t = 0$, dynamic solution can be obtained without constraint of the boundary condition. However, the Dirichlet boundary condition can make the numerical system more stable when an asymptotic steady state is approached.

4.5.4 Approximations for a Physiological Saline Solution

In most bio-media, the ionic composition is dominated by a buffered saline which sets the osmotic pressure [43]. Various cation and anions such as K^+, Ca^{2+} and PO_4^{3-} are present in significantly lower concentration. Phosphate-buffered-saline (PBS) is such a common physiological buffer, composed of the ions in Table 4-2.

Table 4-2 Composition in typical biological buffers such as PBS

	Concentration (mM or mmol/L)	Concentration (g/L)
NaCl	137	8.0
KCl	2.7	0.2
Na_2HPO_4	10	1.42
KH_2PO_4	1.8	0.24
HCl	pH = 7.4	

In the PBS, the relative cation concentrations show $n_K << n_{Na}$, and anions $n_{PO4} << n_{Cl}$. The ebbed diffusivity of the minority ion concentrations in Eq. 3.8 can be approximated by:

$$D_K \cong D_{K0} \frac{1 - a_{Na}^3 n_{Na}}{\left(1 + \left(A_{Na} a_{Na} n_{Na}\right)^m\right)^{1/m}} \qquad (4.11)$$

$$D_{PO4} \cong D_{PO40} \frac{1 - a_{Cl}^3 n_{Cl}}{\left(1 + \left(A_{Cl} a_{Cl} n_{Cl}\right)^m\right)^{1/m}} \qquad (4.12)$$

It is important to note, however, that ions with a higher volumetric valency = z/a^3 can have a smaller total energy in the vicinity of the Steric layer, and this will determine the eventual steady state. The assumption that $n_K << n_{Na}$ should not be made close to the Steric layer, and Eq. 3.8 should be used during the transient, instead of the simplified Eq. 4.11. The Steric layer composition change will take much longer time than in the conventional diffusive layer (where $n << 1/a^3$), as the diffusivity and

mobility approach to zero. Further careful design of experiments is needed to see whether this is the main reason for slow drift in non-amperometric chemical sensing, which had been regarded as one of the major limitations of this approach.

4.6 Experimental Observations

Of primary concern is the effectiveness of the SPEEDD model in the prediction and analysis of electrochemical sensors. As the area in which we look to improve understanding is in higher potential, higher frequency interfacial measurements, pulsed based measurements will provide the greatest initial insight. The clearest expression of the model in this experiment will be in the transient currents seen immediately after the pulse transitions, or as the double layer forms and reorganizes. The expectation is that the interplay of multiple ionic species of the same valency competing for space in the steric layer will take longer to reorganize, leading to a longer tail in the current decay, and a further deviation from the exponential current behavior expected at low (on the order of a few kT) pulses. The simulation and experimental data exploring these phenomena are shown in Figures 4.6 and 4.7.

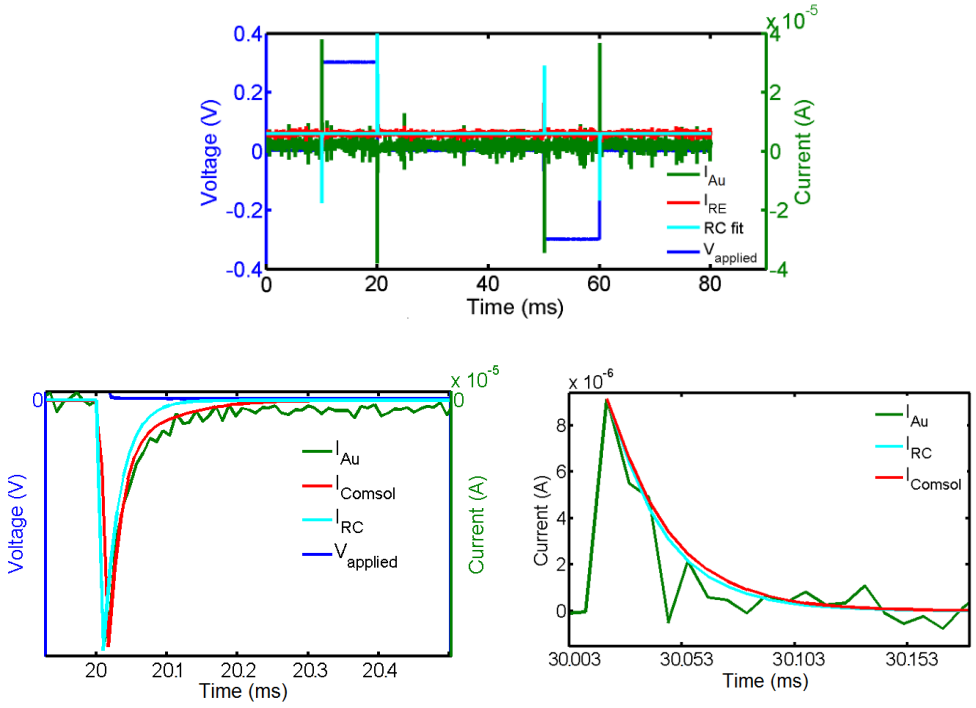

Figure 4.6 (Top) Full view of the 300mV bipolar pulsed experiment (RE and Au represent measurements from the reference electrode and gold electrode respectively, and are inverses of each-other minus an offset from the Keithley 4200 measuring unit. Only one is shown in future graphs). (Bottom Left) Zoomed view of the transition between neutral (excepting the built in potential difference) and negative surface potential. (Bottom Right) Zoomed view of transient currents and simulation resulting from a 70mV applied potential.

The ebbed diffusivity causes the addition of the tail to the exponential, more accurately modeling the experimental data, while a single time constant RC fits the data well, and is also the result of the SPEEDD simulation. Exploring the differences in these tail behaviors is key to the model, and further experimental examples are shown in Figure 4.7.

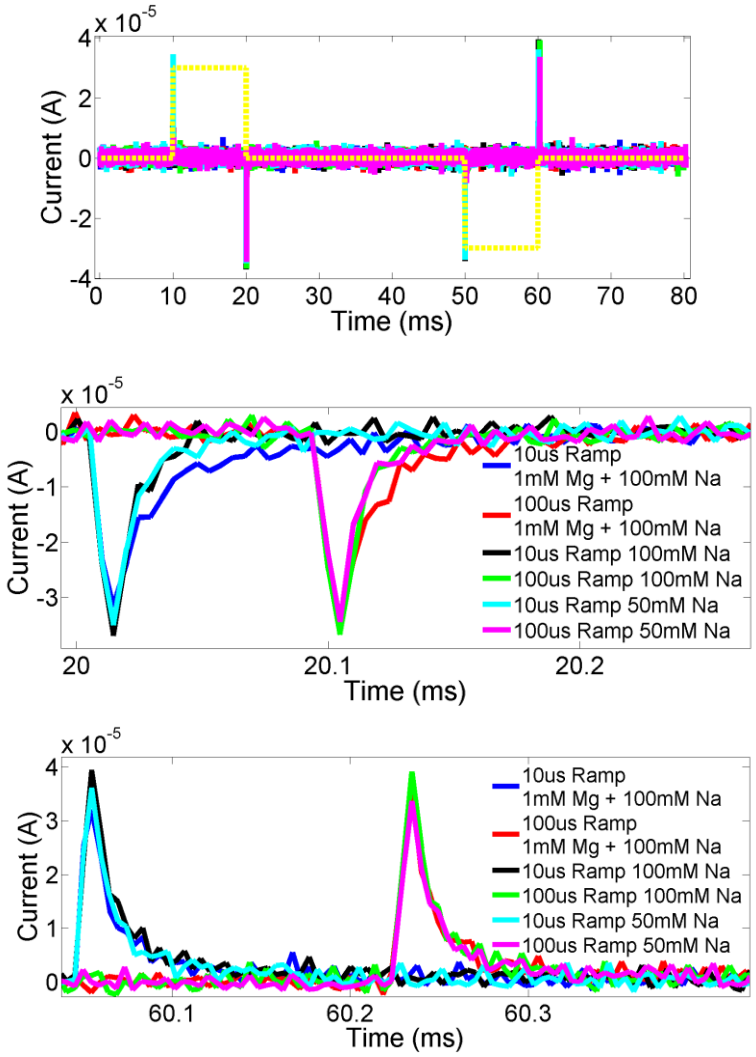

Figure 4.7 Experimental data for NaCl and $MgCl_2$ saline solutions of various molarities, combinations and ramp rates. (Top) Experimental data for a 300mV 10ms bipolar pulse, with initial ramp rates of 10µs and 100µs (yellow dotted lines). The different initial ramp rates may alter the composition of the double layer based on the relative mobilities and energetic favorability. (Middle): zoomed view of currents as the cation steric layer dissipates from the surface as the electrode potential difference returns to zero. The saline solution with 1mM $MgCl_2$ mixed with 100mM NaCl shows a longer decay current than the solution with only 100mM NaCl, as the less concentrated, lower mobility, but more energetically favorable Mg^{+2} moves away from the surface. (Bottom) zoomed

view of currents as the anion steric layer dissipates from the surface. As this is composed of Cl^- for all solutions, no change is seen in the transient current profile, but the same increase in current for higher salinity is clear.

Examining the bipolar pulse data for saline mixtures of different ramp rates allows for further insight into the features we look to observe. It is clear that the addition of Mg^{+2} to the mixture, even in a small concentration, significantly affects the tail of the transient current, while altering the concentration of the Na^+ does not have a strong effect. Altering the ramp rates on the transitions from 0→±300mV from 10μs to 100μs (with 10μs ramp returns to 0V) does not affect the transient current, though may affect the double layer composition in solutions containing low mobility but highly energetically favorable ions ro compounds. In addition, these affects appear clear when compared to the Cl^- curves which show no change under any of the experimental conditions. The increased saline concentration leads to a higher transient current in all cases, but a limited

A mechanism for this effect can be understood from the concentration profiles available from the SPEEDD simulation, shown in Figure 4.8. The long time scale reordering of the interfacial steric layer contributes to the longer tail current.

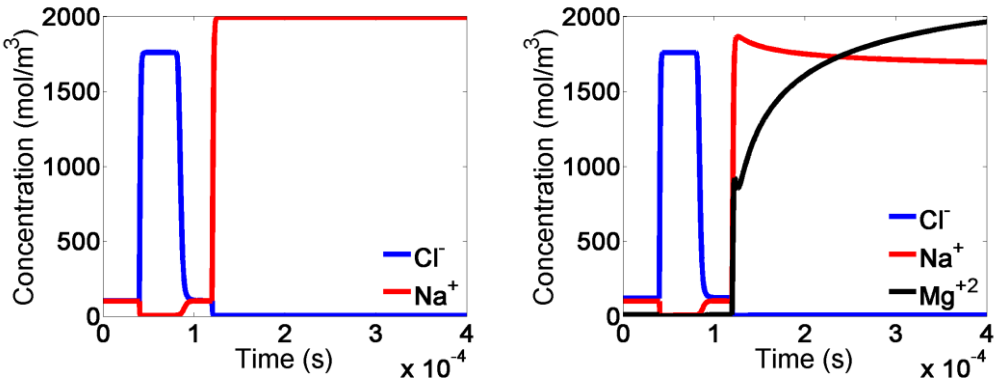

Figure 4.8 Interface Concentration profiles for 100mM NaCl (left) and 100mM NaCl + 10mM $MgCl_2$ subject to a 300mV anodic pulse followed by a 300mV cathodic pulse. For the mono-cation electrolyte, the concentrations rapidly approach steady state values, while the poly-cation electrolyte requires a long equilibration time as the higher mobility Na^+ initially forms the steric layer, and is then replaced by the more energetically favorable Mg^{+2}.

4.7 Conclusion

The SPEEDD model succeeds in accurately modeling the transient currents seen from a pulsed waveform, and improves on the accuracy of a single time constant fitting. While relying on parameters seemingly difficult to access experimentally, the parameter extraction scheme has enough redundancy to lend confidence to the results.

CHAPTER 5

FABRIC BASED RFID ANTENNAE AND SYSTEMS

5.1 Introduction

For smart clothing integration with the wireless system based on radio frequency (RF) backscattering, we demonstrate an ultra-high frequency (UHF) antenna constructed from embroidered conductive threads. Sewn into a fabric backing, the T-match antenna design mimics a commercial UHF RFID tag, which was also used for comparative testing. Bonded to the fabric antenna is the integrated circuit chip dissected from another commercial RFID tag, which allows for testing the tags under normal EPC Gen 2 operating conditions. We find that, despite of the high resistive loss of the antenna and inexact impedance matching, the fabric antenna works reasonably well as a UHF antenna both in standalone RFID testing, and during variety of ways of wearing under sweaters or as wristbands. The embroidering pattern does not affect much the feel and comfort from either side of the fabrics by our sewing method.

5.2 Motivation

To enable wireless sensing and data transmission of useful wearer conditions, integration of battery-free sensor tags unto clothing is technically feasible and affordable. Due to wearing and laundry considerations, passive UHF RFID tags such as those employed in item-level inventory monitoring offer many advantages in

garment manufacturing and care. Conventional RFID tags are often built on a paper or plastic substrate with laminated plastic covering an aluminum antenna and a small integrated-circuit (IC) chip. This packaging is cost effective for logistics-controlled tags, but does not integrate well for wear comfort and for laundry durability. Printed aluminum antennas and the non-fabric substrate cause additional limits in normal wear, aesthetic designs, and washing/drying options. We minimize the amount of non-fabric materials in the tag by constructing the antenna using conductive threads, embroidered directly onto the fabric[56]. Conductive epoxy was chosen as the interconnect method to the IC chip to minimize the impact on read distance over the course of wear and wash cycles [40].

5.3 Fabrication

Conductive threads were used to embroider a UHF T-match antenna pattern onto a piece of polyester fabric (Figure 5.1). The conductive thread has a single-thread resistivity of .7Ω/cm, with strand-to-strand resistance dependent on the tightness of the stitching. Double-sided stitching was used to decrease the resistance, and the total DC resistance across the antenna was around 51Ω. While dense stitching has been reported to cause unexpected losses [57], this was deemed necessary to counteract the contact resistance to the IC chip, measured at 47Ω. An RFID tag IC chip was cut from a commercial tag, and connected to the antenna via conductive epoxy after removing the initial plastic passivation and adhesive layers with a two-hour toluene submersion.

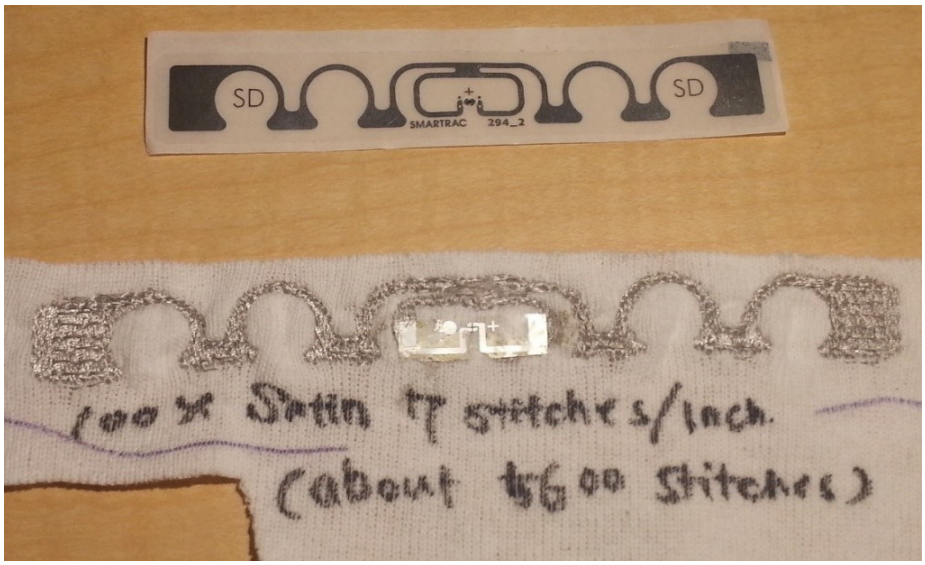

Figure 5.1 Photograph of commercial Smartrac® ShortDipole UHF RFID tag (top) next to the fabric based antenna with an IC chip connected in the center (bottom). The fabric antenna, while 15% larger and 300x higher resistance, still functioned similarly out to 2.5m.

5.4 Testing

The fabric tag was tested using an Impinj Speedway® R420 reader with an output power of 32.5dBm and a Laird S9028PCR panel antenna, side by side with a commercial UHF EPC paper-based tag. The two tags performed very similarly out to 2.5m, as shown in Figure 5.2, with typical oscillation of received signal strength indicator (RSSI) for indoors environment. To study the perspiration influence, 100mM saline solution was used to simulate sweat. Partial saline wetting decreased RSSI for 6 – 10dB probably due to mismatched impedance, but the embroidered tag remains functional at a reduced distance.

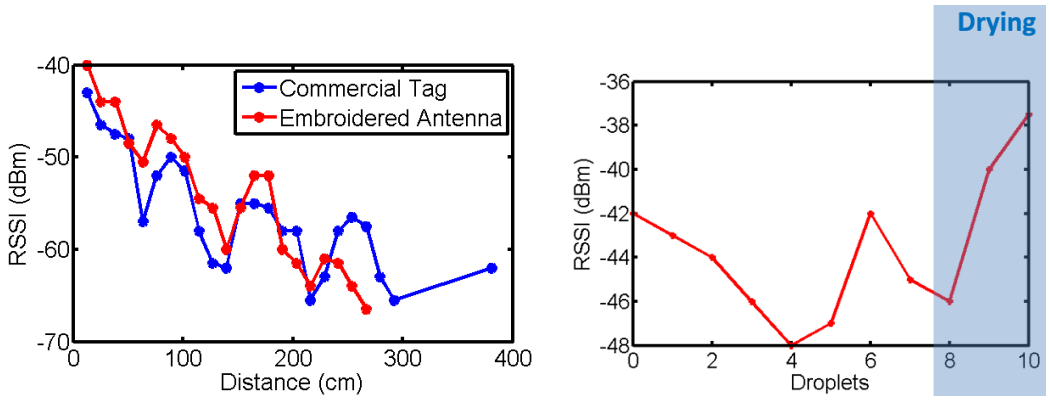

Figure 5.2 Left) Received signal strength indicator (RSSI) vs. reading distance for both the embroidered fabric tag (red) and the commercial control tag (blue). Comparable performance was achieved out to 2.5m, before signal was lost for the embroidered antenna. Right) Embroidered antenna RSSI response to 100mM NaCl saline solution. Droplets were added until full saturation at droplet 7, after which recordings were taken until fully dry at marker 10. Partial wetness decreased signal strength, which had worse performance than full saline saturation probably due to impedance mismatch. Returning to a dry state showed no lasting effects.

The fabric tag was also tested on the chest [49], under a coat on the chest, and on the wrist as a wristband. While significant attenuation was noted (specifically with the wristband configuration, which was only readable out to 30cm due to the reduced radar cross section), the fabric tag did function in all wearable cases (Table 5-1) with EPC protocols.

Table 5-1 Received Signal Strength Intensity during wear

Distance (cm)	**RSSI On Shirt (dBm)**	**RSSI Under Sweater (dBm)**
30	–44	–59
90	–49	–64
150	–55.5	–64.5

The antenna impedance at RF frequencies is the most important parameter in terms of assessing the prototype to improve future designs. As discussed previously though, making an effective contact to the antenna is difficult. To best simulate the UHF RFID implementation, an SMA cable was cut, and the grounding soldered to one piece of copper foil, while the signal line was soldered to another. The modified cable was then attached to the antenna with the same conductive epoxy used to attach the IC. The same setup was created for a commercial tag, with its IC cut out. The frequency was swept from 600MHz to 1.2GHz, resulting in the Smith chart shown in Figure 5.3.

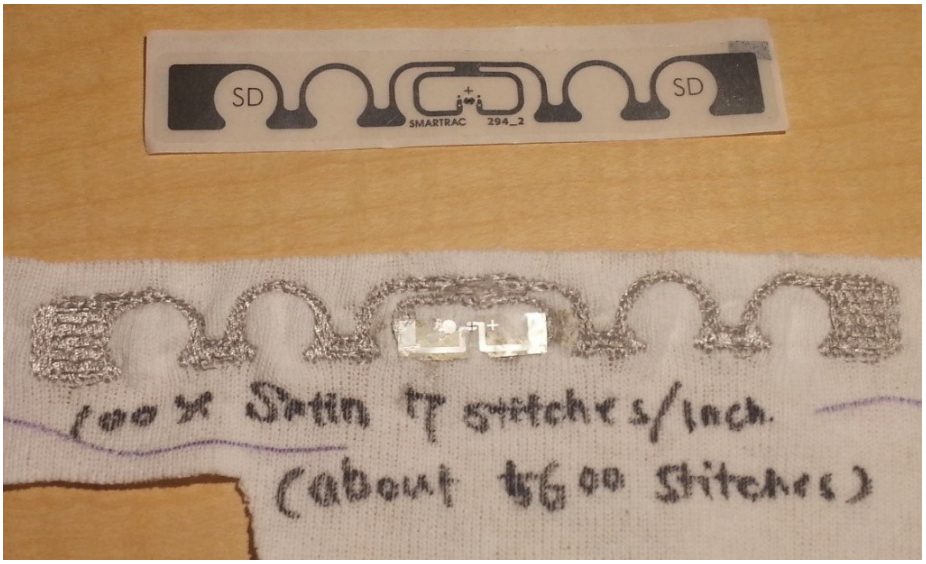
SD
SD
SMARTRAC 294_2
(00 x Satin 11 stitches/inch.
(about 1600 Stitches)

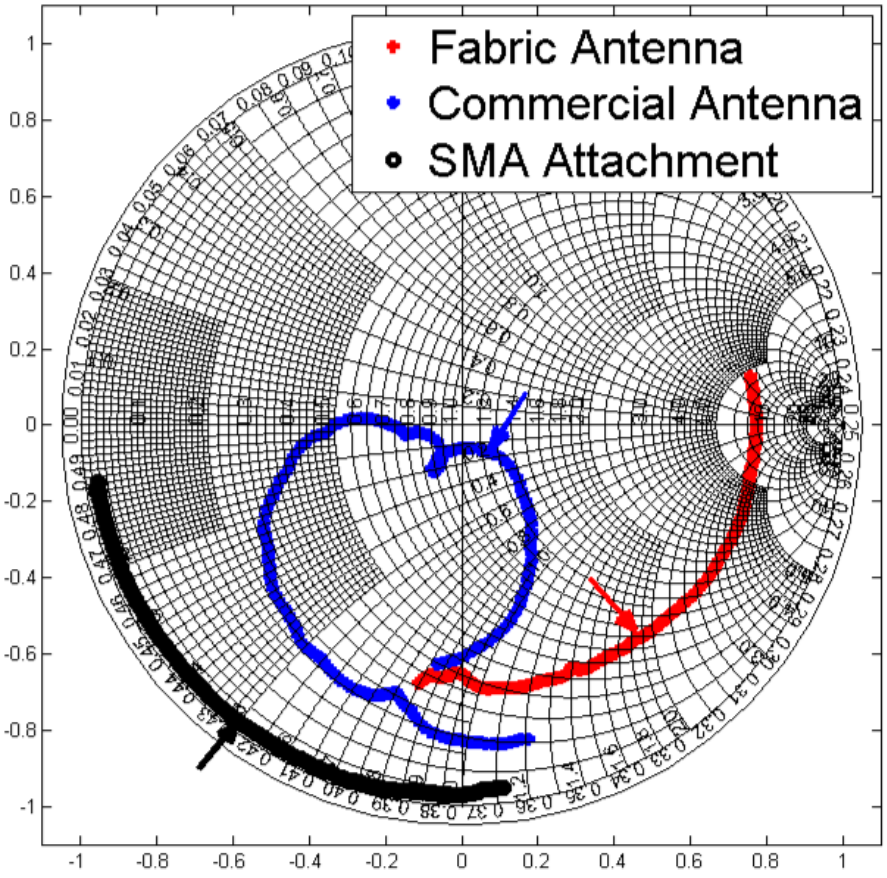
Fabric Antenna
Commercial Antenna
SMA Attachment
1
0.8
0.6
0.4
0.2
0
-0.2
-0.4
-0.6
-0.8
-1
-1
-0.8
-0.6
-0.4
-0.2
0
0.2
0.4
0.6
0.8
1

Figure 5.3 Left) Received signal strength indicator (RSSI) vs. reading distance for both the embroidered fabric tag (red) and the commercial control tag (blue). Comparable performance was achieved out to 2.5m, before signal was lost for the embroidered antenna. Right) Embroidered antenna RSSI response to 100mM NaCl saline solution. Droplets were added until full saturation at droplet 7, after which recordings were taken until fully dry at marker 10. Partial wetness decreased signal strength, which had worse performance than full saline saturation probably due to impedance mismatch. Returning to a dry state showed no lasting effects.

While the real impedance of the fabric antenna is close to the 50Ω match intended at 900Mhz, the reactance is far from matched, indicating a poor inductive match attempt with the T-matching structure.

5.5 Conclusions

In the expanding field of smart clothing and wearable devices, the fully integrated fiber based antenna is sure to be a staple component. The prototype silver coated thread embroidered antenna explored here shows both the promise and difficulties of the integration. Impedance matching and tuning will likely need to be implemented on the integrated circuit, predictive modeling of the antenna behavior, particularly the inter-thread electrical properties, is still at its infancy. However even with the poor matching and high resistance, the antenna can function, and further development can only improve read distance and strength.

CHAPTER 6

COMPARISONS AND ANALYSIS

6.1 Comparison to Other Models

The modeling of electrolyte sensors and interfaces is not a new field, and any new model not only good support from experiment, but convincing reasons to choose it over past models. Having discussed the experimental verifications in chapters 2, 3 and 4, a comparison to other options is considered in Table 6-1.

Table 6-1 Model Comparisons

	φ	f	Dynamics	Prediction	Computation	Intuitive
GCS/PB	Small	Low	No	Yes	Very Fast	Excellent
SMPB	Small/Large	Low	No	Yes	Fast	Good
Circuit	N/A	High	Yes*	No	Very Fast	Excellent
MD	Small/Large	Highest	Yes	Yes	Very Slow	Poor
SPEEDD	Small/Large	High	Yes	Yes	Medium	Average

* Can only give integrated information, such as net current.

The comparison of potential accuracy (φ) concerns what level of DC bias for which the model is accurate. The GCS or PB models, without a transitional steric layer, will not accurately model potentials larger than ~$5V_T$. The Circuit model with a CPE, being a lumped model, is integrated spatially and thus gives no voltage profile. The SMPB,

MD, and SPEEDD models will give accurate voltage profiles at both small and large potentials. It must be noted that none of these potentials will be much over $^{+}/_{-}$ 1V, as we are dealing with non-Faradaic systems, and electrolysis of water will occur at any 1.23V difference in the system [58].

Accuracy with respect to frequency is assessed next. Being static in nature, both the GCS/PB models, and the SMPB models will be accurate only at lower frequencies, where the system can reach a steady state in between measurements. The Circuit and SPEEDD models are both time varying in nature and can function at high frequencies, so long as the charge carriers function as discrete objects (although a more complex Circuit model can account for these [24]). The MD simulation offers the highest frequency fidelity, with an ability to deal with the modes of intramolecular bonds at GHz frequencies [23].

The question of dynamic information, or time varying information is closely related to frequency. Again, the GCS/PB and SMPB models with their steady state nature, will not give details on the dynamics of the system. The Circuit model will deliver integrated information such as net current through the system, but no information on the changing composition of any spatial parameters. The SPEEDD and MD models can give dynamic information about all parameters in the system both spatially and temporally.

Predictive ability of the models addresses, given a known complex electrolyte mixture, what is the capability of the model to predict the parameters of the system. The GCS/PB and SMPB systems, while most accurate for simple electrolytes, have

the capability of predicting complex electrolyte behavior, though with diminished accuracy. The Circuit model can make a prediction based off total molarity of the solution, but is more accurate as an analysis tool than a predictive one. An MD simulation can cope with complex electrolytes, though it may significantly increase computation time. The SPEEDD model is designed to address complex polyelectrolyte systems, and will increase in computation time only marginally.

Computational complexity concerns how long it will take to run a simulation of a complex electrolyte system. The concern here is the ability of a model to be used iteratively in the design phase for a device or experiment. The GCS/PB model is by far the fastest, and can even be analytically solved for some electrolytes. The SMPB model likewise is similar, though the Steric modification will increase computation time. The SPEEDD model will be slightly slower than a pure SMPB model, as more terms are dependent on both Steric terms and each other. In addition, being temporally varying in nature, each time solution will take on the order of an SMPB solution, making slower proportionally to the length of the experiment being simulated. The Circuit model, without the cumbersome geometric solutions, will finish as any other SPICE model, which for the analysis here is on the order of the GCS/PB models. The MD simulation will take far, far longer than any of the other models here, and it is this constraint more than almost any other that makes it unviable for design use.

Lastly the intuitive nature of the models is assessed. Examining from the point of view of someone using the tool without the understanding required to create it, with the understanding of an undergraduate level course in electrochemistry and circuit

theory. The GCS/PB models, along with the Circuit model, will be the most accessible. The concepts and mathematics are the simplest of those described here, and can give build an intuition to how the system will respond to different electrolytes. The SMPB, being the next extension, can become intuitive after a grasp of the GCS/PB model is achieved, and lends further insight into the system, but will naturally be more difficult to grasp immediately. The SPEEDD model increases in complexity in a similar degree, and (as intuition is a difficult concept to quantify) will be taken here as the average difficulty. This is to say that the SPEEDD model has many parameters changing over both time and space with respect to each other, and to gain an intuitive understanding of what will happen when a given parameter changes takes a good deal of effort. The MD simulation is simultaneously intuitive to understand at the smallest level (it assesses the molecule-molecule or group-to-group interactions using inter-molecular forces as opposed to statistical mechanics), and also the opaquest in terms of intuition. This is somewhat the point of the model, however, as seeing emergent phenomena come from simple interactions is one of the great virtues of MD simulations.

6.2 SPEEDD Model Improvements and Additions

There are other physical parameters available to the SPEEDD model which have yet to be integrated. The boundary conditions considered so far are for a simple non-Faradaic electrode, and a single species reference electrode. There can be other phenomena in solution, such as the generation/recombination term (or reaction rate) R_i

which has been set to zero for this initial analysis. For experimental setups where a species may be added to solution and initiate a chemical reaction, this term would be absolutely required. In addition, the Steric term a_i could be amended to a different geometry (such as a sphere, or other shape with known packing style), to deliver a more physically precise parameter.

Little work has been done at this point exploiting the new model in terms of response to complex electrical signals. Pulsed voltages have been the testing waveform of choice, but the model is capable of handling any arbitrary waveform. In particular, the CV experiment can be duplicated exactly in simulation, with AC perturbations on top of a DC bias to create another hierarchical parameter extraction scheme.

Noise considerations have also not been explicitly added to the model. While injecting input noise at the sensing gate of the transistor as per other works [59-61] will be the first step, a more integrated model will involve noise sources built into the partial differential equations themselves. The idea being that as the model is non-lumped in nature, variability can be built into the diffusivity correction which will cause an uncertainty in the concentration at a given position. This gives a source of thermal noise, but will require further consideration in terms of implementation, and other noise sources (particularly frequency dependent) will need to be incorporated as well.

It has recently become experimentally clear that the packing structure of the Steric layer is also a function of the applied voltage [62]. This voltage dependence may

account for some hysteresis seen in the CV's of chapter 2. The effect on the SPEEDD model would be a voltage dependent ionic size $a_i(\varphi)$.

6.3 Conclusion

In this work, I have endeavored to show the uses of non-Faradaic electrochemical sensors, their models, and introduced a new model to try to enhance the usefulness of this tool. As the biotechnology industry expands, personalized medicine blossoms, and the semiconductor industry continues to change how we live and interact, it is my hope that these sensors can find further uses to enhance the quality of human life.

REFERENCES

[1] P. S. Singh, "From Sensors to Systems: CMOS-Integrated Electrochemical Biosensors," *Access, IEEE,* vol. 3, pp. 249-259, 2015.

[2] P. Bergveld, "Development of an Ion-Sensitive Solid-State Device for Neurophysiological Measurements," *Biomedical Engineering, IEEE Transactions on,* vol. BME-17, pp. 70-71, 1970.

[3] M. Wolf, R. Gulich, P. Lunkenheimer, and A. Loidl, "Relaxation dynamics of a protein solution investigated by dielectric spectroscopy," *Biochimica et Biophysica Acta (BBA) - Proteins and Proteomics,* vol. 1824, pp. 723-730, 2012.

[4] T. Shibata and T. Ohmi, "A functional MOS transistor featuring gate-level weighted sum and threshold operations," *Electron Devices, IEEE Transactions on,* vol. 39, pp. 1444-1455, 1992.

[5] A. J. Bard and L. R. Faulkner, *Electrochemical methods: fundamentals and applications* vol. 2: Wiley New York, 1980.

[6] H. V. Helmholtz, "Studien über electrische Grenzschichten," *Annalen der Physik,* vol. 243, pp. 337-382, 1879.

[7] S. E. Moulton, J. N. Barisci, A. Bath, R. Stella, and G. G. Wallace, "Studies of double layer capacitance and electron transfer at a gold electrode exposed to protein solutions," *Electrochimica Acta,* vol. 49, pp. 4223-4230, 2004.

[8] M. Labib, M. Hedström, M. Amin, and B. Mattiasson, "A capacitive immunosensor for detection of cholera toxin," *Analytica chimica acta,* vol. 634, pp. 255-261, 2009.

[9] R. E. G. van Hal, J. C. T. Eijkel, and P. Bergveld, "A novel description of ISFET sensitivity with the buffer capacity and double-layer capacitance as key parameters," *Sensors and Actuators B: Chemical,* vol. 24, pp. 201-205, 1995.

[10] R. S. Hansen, D. J. Kelsh, and D. H. Grantham, "THE INFERENCE OF ADSORPTION FROM DIFFERENTIAL DOUBLE LAYER CAPACITANCE MEASUREMENTS. II. DEPENDENCE OF SURFACE CHARGE DENSITY ON ORGANIC NONELECTROLYTE SURFACE EXCESS1,2," *The Journal of Physical Chemistry,* vol. 67, pp. 2316-2326, 1963/11/01 1963.

[11] I. Borukhov, D. Andelman, and H. Orland, "Steric Effects in Electrolytes: A Modified Poisson-Boltzmann Equation," *Physical Review Letters,* vol. 79, pp. 435-438, 1997.

[12] M. S. Kilic, M. Z. Bazant, and A. Ajdari, "Steric effects in the dynamics of electrolytes at large applied voltages. I. Double-layer charging," *Physical Review E,* vol. 75, p. 021502, 2007.

[13] R. Morrow, D. R. McKenzie, and M. M. M. Bilek, "The time-dependent development of electric double-layers in saline solutions," *Journal of Physics D: Applied Physics,* vol. 39, p. 937, 2006.

[14] Y. Ma, C. Wen, R. Zeng, M. Xu, J. Pan, and D. Wu, "Compact modelling and simulation of extended-gate ion-sensitive field-effect-transistor," in *Solid-State and Integrated Circuit Technology (ICSICT), 2014 12th IEEE International Conference on*, 2014, pp. 1-3.

[15] T. M. Abdolkader, "A numerical simulation tool for nanoscale ion-sensitive field-effect transistor," *International Journal of Numerical Modelling: Electronic Networks, Devices and Fields,* 2016.
[16] K. Jayant, K. Auluck, M. Funke, S. Anwar, J. B. Phelps, P. H. Gordon*, et al.*, "Programmable ion-sensitive transistor interfaces. I. Electrochemical gating," *Physical Review E,* vol. 88, p. 012801, 2013.
[17] K. Jayant, K. Auluck, M. Funke, S. Anwar, J. B. Phelps, P. H. Gordon*, et al.*, "Programmable ion-sensitive transistor interfaces. II. Biomolecular sensing and manipulation," *Physical Review E,* vol. 88, p. 012802, 2013.
[18] K. Jayant, K. Auluck, S. Rodriguez, Y. Cao, and E. C. Kan, "Programmable ion-sensitive transistor interfaces. III. Design considerations, signal generation, and sensitivity enhancement," *Physical Review E,* vol. 89, p. 052817, 2014.
[19] L. Bousse and P. Bergveld, "The role of buried OH sites in the response mechanism of inorganic-gate pH-sensitive ISFETs," *Sensors and Actuators,* vol. 6, pp. 65-78, 1984/09/01 1984.
[20] A. Topkar and R. Lal, "Ionic penetration into reoxidized nitrided oxides in electrolyte-oxide-semiconductor structures," *Thin Solid Films,* vol. 259, pp. 259-263, 1995/04/15 1995.
[21] P. H. Gordon, K. Jayant, J. B. Phelps, and E. C. Kan, "Capacitive control of an ISFET using dielectric coated electrodes," in *Sensors, 2013 IEEE*, 2013, pp. 1-4.
[22] M. Gouy, "Sur la constitution de la charge electrique a la surface d'un electrolyte," *J. Phys. Theor. Appl.,* vol. 9, pp. 457-468, 1910.
[23] E. Barsoukov and J. R. Macdonald, *Impedance spectroscopy: theory, experiment, and applications*: John Wiley & Sons, 2005.
[24] J. R. Macdonald, "Impedance spectroscopy: Models, data fitting, and analysis," *Solid State Ionics,* vol. 176, pp. 1961-1969, 2005.
[25] M. V. Fedorov, N. Georgi, and A. A. Kornyshev, "Double layer in ionic liquids: The nature of the camel shape of capacitance," *Electrochemistry Communications,* vol. 12, pp. 296-299, 2010.
[26] R. L. Stoop, M. Wipf, S. Müller, K. Bedner, I. A. Wright, C. J. Martin*, et al.*, "Competing surface reactions limiting the performance of ion-sensitive field-effect transistors," *Sensors and Actuators B: Chemical,* vol. 220, pp. 500-507, 2015.
[27] M. Y. Kiriukhin and K. D. Collins, "Dynamic hydration numbers for biologically important ions," *Biophysical chemistry,* vol. 99, pp. 155-168, 2002.
[28] M. Grattarola, G. Massobrio, and S. Martinoia, "Modeling H+-sensitive FETs with SPICE," *Electron Devices, IEEE Transactions on,* vol. 39, pp. 813-819, 1992.
[29] K. Lee, P. R. Nair, A. Scott, M. A. Alam, and D. B. Janes, "Device considerations for development of conductance-based biosensors," *Journal of Applied Physics,* vol. 105, p. 102046, 2009.
[30] D. Landheer, G. Aers, W. McKinnon, M. Deen, and J. Ranuarez, "Model for the field effect from layers of biological macromolecules on the gates of metal-

oxide-semiconductor transistors," *Journal of Applied Physics,* vol. 98, p. 044701, 2005.
[31] D. Landheer, W. R. McKinnon, G. Aers, W. Jiang, M. J. Deen, and M. W. Shinwari, "Calculation of the response of field-effect transistors to charged biological molecules," *Sensors Journal, IEEE,* vol. 7, pp. 1233-1242, 2007.
[32] H. J. Jang and W. J. Cho, "Performance Enhancement of Capacitive-Coupling Dual-gate Ion-Sensitive Field-Effect Transistor in Ultra-Thin-Body," *Scientific Reports,* vol. 4, Jun 2014.
[33] O. Stern, "The theory of the electrolytic double-layer," *Z. Elektrochem,* vol. 30, pp. 1014-1020, 1924.
[34] P. H. R. Alijó, F. W. Tavares, E. C. Biscaia Jr, and A. R. Secchi, "Steric effects on ion dynamics near charged electrodes," *Fluid Phase Equilibria,* vol. 362, pp. 177-186, 2014.
[35] I. Siretanu, D. Ebeling, M. P. Andersson, S. L. S. Stipp, A. Philipse, M. C. Stuart, *et al.*, "Direct observation of ionic structure at solid-liquid interfaces: a deep look into the Stern Layer," *Scientific Reports,* vol. 4, p. 4956, 2014.
[36] L. Wang, C. Zhao, M. H. G. Duits, F. Mugele, and I. Siretanu, "Detection of ion adsorption at solid–liquid interfaces using internal reflection ellipsometry," *Sensors and Actuators B: Chemical,* vol. 210, pp. 649-655, 2015.
[37] Y. Taur and T. H. Ning, *Fundamentals of modern VLSI devices*: Cambridge university press, 2013.
[38] Y. Liu, D. E. Huber, V. Tabard-Cossa, and R. W. Dutton, "Descreening of field effect in electrically gated nanopores," *Applied Physics Letters,* vol. 97, p. 143109, 2010.
[39] B. D. Storey and M. Z. Bazant, "Effects of electrostatic correlations on electrokinetic phenomena," *Physical Review E,* vol. 86, p. 056303, 2012.
[40] C. J. Fell and H. P. Hutchison, "Diffusion coefficients for sodium and potassium chlorides in water at elevated temperatures," *Journal of Chemical & Engineering Data,* vol. 16, pp. 427-429, 1971.
[41] V. Vitagliano and P. Lyons, "Diffusion coefficients for aqueous solutions of sodium chloride and barium chloride," *Journal of the American Chemical Society,* vol. 78, pp. 1549-1552, 1956.
[42] M. Z. Bazant, M. S. Kilic, B. D. Storey, and A. Ajdari, "Towards an understanding of induced-charge electrokinetics at large applied voltages in concentrated solutions," *arXiv preprint arXiv:0903.4790,* 2009.
[43] M. Kaisti, Q. Zhang, A. Prabhu, A. Lehmusvuori, A. Rahman, and K. Levon, "An Ion-Sensitive Floating Gate FET Model: Operating Principles and Electrofluidic Gating," *Ieee Transactions on Electron Devices,* vol. 62, pp. 2628-2635, Aug 2015.
[44] P. Bergveld, "Thirty years of ISFETOLOGY: What happened in the past 30 years and what may happen in the next 30 years," *Sensors and Actuators B: Chemical,* vol. 88, pp. 1-20, 2003.
[45] P. H. Gordon, K. Jayant, Y. Cao, K. Auluck, J. Phelps, and E. C. Kan, "Critical Assessment on Modeling and Design of Nonfaradaic CMOS Electrochemical Sensing," *IEEE Sensors Journal,* vol. 16, pp. 3367-3373, 2016.

[46] A. Poghossian and M. J. Schöning, "Label-Free Sensing of Biomolecules with Field-Effect Devices for Clinical Applications," *Electroanalysis,* vol. 26, pp. 1197-1213, 2014.
[47] M. S. Kilic, M. Z. Bazant, and A. Ajdari, "Steric effects in the dynamics of electrolytes at large applied voltages. II. Modified Poisson-Nernst-Planck equations," *Physical Review E,* vol. 75, p. 021503, 2007.
[48] D. L. Chapman, "LI. A contribution to the theory of electrocapillarity," *The London, Edinburgh, and Dublin Philosophical Magazine and Journal of Science,* vol. 25, pp. 475-481, 1913.
[49] D. C. Grahame, "The Electrical Double Layer and the Theory of Electrocapillarity," *Chemical Reviews,* vol. 41, pp. 441-501, 1947/12/01 1947.
[50] M. Springer, A. Korteweg, and J. Lyklema, "The relaxation of the double layer around colloid particles and the low-frequency dielectric dispersion: Part II. Experiments," *Journal of Electroanalytical Chemistry and Interfacial Electrochemistry,* vol. 153, pp. 55-66, 1983.
[51] J. R. MacDonald, "Double layer capacitance and relaxation in electrolytes and solids," *Transactions of the Faraday Society,* vol. 66, pp. 943-958, 1970.
[52] P. Debye and E. Hückel, "De la theorie des electrolytes. I. abaissement du point de congelation et phenomenes associes," *Physikalische Zeitschrift,* vol. 24, pp. 185-206, 1923.
[53] K. Letchworth-Weaver and T. A. Arias, "Joint density functional theory of the electrode-electrolyte interface: Application to fixed electrode potentials, interfacial capacitances, and potentials of zero charge," *Physical Review B,* vol. 86, p. 075140, 2012.
[54] A. Thanachayanont, "A 1-V, 330-nW, 6-Bit Current-Mode Logarithmic Cyclic ADC for ISFET-Based Digital Readout System," *Circuits Systems and Signal Processing,* vol. 34, pp. 1405-1429, May 2015.
[55] E. J. F. Dickinson, H. Ekström, and E. Fontes, "COMSOL Multiphysics®: Finite element software for electrochemical analysis. A mini-review," *Electrochemistry Communications,* vol. 40, pp. 71-74, 3// 2014.
[56] B. Lertanantawong, A. P. O'Mullane, W. Surareungchai, M. Somasundrum, L. D. Burke, and A. M. Bond, "Study of the Underlying Electrochemistry of Polycrystalline Gold Electrodes in Aqueous Solution and Electrocatalysis by Large Amplitude Fourier Transformed Alternating Current Voltammetry," *Langmuir,* vol. 24, pp. 2856-2868, 2008/03/01 2008.
[57] D. G. Miller, J. A. Rard, L. B. Eppstein, and J. G. Albright, "Mutual diffusion coefficients and ionic transport coefficients lij of magnesium chloride-water at 25.degree.C," *The Journal of Physical Chemistry,* vol. 88, pp. 5739-5748, 1984/11/01 1984.
[58] J. C. Wang, "Realizations of Generalized Warburg Impedance with RC Ladder Networks and Transmission Lines," *Journal of The Electrochemical Society,* vol. 134, pp. 1915-1920, August 1, 1987 1987.
[59] M. Deen, M. Shinwari, J. Ranuárez, and D. Landheer, "Noise considerations in field-effect biosensors," *Journal of Applied Physics,* vol. 100, p. 074703, 2006.

[60] J. Go, P. R. Nair, and M. A. Alam, "Theory of signal and noise in double-gated nanoscale electronic pH sensors," *Journal of Applied Physics,* vol. 112, pp. -, 2012.
[61] A. Hassibi, R. Navid, R. W. Dutton, and T. H. Lee, "Comprehensive study of noise processes in electrode electrolyte interfaces," *Journal of Applied Physics,* vol. 96, pp. 1074-1082, 2004.
[62] Y. Nakayama and D. Andelman, "Differential capacitance of the electric double layer: The interplay between ion finite size and dielectric decrement," *The Journal of Chemical Physics,* vol. 142, p. 044706, 2015.